Direct assessment of the hydraulic structure of the plate boundary at the toe of the Nankai accretionary prism

Joshua Pwavodi, Mai Linh Doan

submitted to *Geophys. J. Int.*

Direct assessment of the hydraulic structure of the plate boundary at the toe of the Nankai accretionary prism

Joshua Pwavodi [1],[2], Mai-Linh Doan [1]

[1] *Univ. Grenoble Alpes, Univ. Savoie Mont Blanc, CNRS, IRD, UGE, ISTerre, 38000 Grenoble, France*

[2] *Ecole et Observatoire des Sciences de la Terre, ITES UMR7063 – CNRS/Université de Strasbourg, 5 rue Rene Descartes 67084 Strasbourg, FRANCE*

SUMMARY

The Nankai Trough is a locus of slow slip, low-frequency earthquakes, and large magnitude ($M_w > 8$) earthquakes. It is usually assumed that high pore pressure contributes substantially to earthquake dynamics. Hence, a thorough understanding of the hydraulic regime of the Nankai accretionary prism is needed to understand this diversity of behaviors. We focus on the toe of the accretionary prism by studying data from Hole C0024A, part of the Nankai Trough Seismogenic Zone Experiment (NanTroSEIZE) project, that intersected the décollement at 813 meters below seafloor (mbsf) about 3 km away from the trench. We contribute to this understanding by innovatively integrating drilling and logging data to derive high-resolution hydraulic profiles along the borehole. A quantitative re-analysis of the variation in the downhole annular pressure monitored during drilling show localized fluid flow from the formation to the borehole in excess of 0.05 m^3/s, especially in the damage zones at the footwall of the décollement. To validate the fluid flow profile, pore pressure was estimated independently from empirical relationships between pore pressure, porosity, and P-wave velocity, obtained from consolidation experiments and Eaton-type methods based on drilling or sonic velocity data. The formation fluids are becoming significantly over-pressurized with depth in the few hundred meters above décollement. The hydraulic profile suggests that the core of the décollement acts as a

barrier inhibiting upward fluid convection, whereas the damage zone acts as an efficient longitudinal channel able to diffuse high pressure from the deeper part of the subduction.

Key words: Nankai Accretionary Prism, Fluid Flow, Pore Fluid Pressure, Tsunami, Downhole Annular Pressure, Drilling

1 INTRODUCTION

Understanding the interplay of fluid flow, high pore pressure, and the resulting decrease in effective stress is key to understanding tectonic deformation and earthquake occurrence in subduction zones (Jaeger, 1971). It is commonly understood that fluids confined at depths and elevated pore pressure influence fault mechanics in subduction zones (Davis et al., 1983; Rubey & Hubbert, 1959; Miller, 2013). There are several sources of fluids identified in subduction zones. They may be introduced in subduction zones as fluid-rich sediments from the incoming plate, that either underthrust or are scrapped off to build up the accretionary prism (Davis et al., 1983). Fluids may also be released by mineral dehydration or sediment compaction (Saffer & Tobin, 2011). In addition to these sources, the fluid distribution is controlled by fluid migration. Fluids can escape through the porous network of rocks or be channeled along fractures or fault zones, whose permeability can be influenced by the maturity of the fault zone architecture (Caine et al., 1996).

The structure of active faults is complex, with features spanning several length scales (Caine et al., 1996). Slip occurs on a thin fault core, sometimes a few centimers wide (Chester et al., 1993), with a differentiated fault gouge, rich in phyllosilicate and hence of low permeability (Faulkner et al., 2010). The damage zone can be a flow path (Doan et al., 2006), however, obtaining an estimate of hydraulic properties (pore pressure, permeability) is difficult (Saffer & Tobin, 2011). Three families of techniques are commonly used to quantify in-situ pore pressure and flow within the accretionary prism, with a particular emphasis on understanding the plate boundary but they don't provide a continuous profile at the metric scale.

A first method combines laboratory consolidation experiments with numerical simulations of the of the accretionary process. Hydro-mechanical properties from cores collected during the consolidation tests are used to calibrate and constrain the numerical models. Such studies have been done for 1D (Shi & Wang, 1985; Gamage & Screaton, 2006; Daigle & Piña, 2016; Skarbek & Saffer, 2009), 2D (Rowe et al., 2012), and 3D geometries (Screaton & Ge, 1997; Spinelli et al., 2006). This approach suffers from strong assumptions about the representativeness of the few core samples on which the consolidation experiments were carried out. Additionally, numerical models of the building of accretionary prisms are large-scale models, with mesh size a few kilometers wide. Fine structures are then

difficult to introduce. Hence, it is difficult for these models to predict the high-resolution structures that the borehole crosses. In particular, it is difficult to model the internal structure of fault zones within the accretionary prism.

A second method uses of long term borehole monitoring systems to provide *in situ* measurements of elevated pore-fluid pressures, fluid flow, fluid chemistry, and temperature variation (Davis & Becker, 1994; Henry, 2000; Jannasch et al., 2003; Becker & Davis, 2005; Kastner et al., 2006; Sawyer et al., 2008; Wheat et al., 2010; Bekins et al., 2011; Fisher et al., 2011; Hammerschmidt et al., 2013; Kinoshita et al., 2018). Although this method gives accurate estimates of pressure and flow, it is limited to a discrete depth intervals and hence does not capture a continuous log of hydraulic heterogeneities with depth in the borehole.

A third method is based on seismic velocity (Tobin & Saffer, 2009; Tsuji et al., 2008). Strong calibration based on samples is needed to convert seismic anomalies into hydrogeological quantities. These calibrations are performed on core samples, with the same issue of representativeness as for the first type of study. Furthermore, offshore seismic reflection profiles have coarse resolution (wavelength about $>$ 10 m). All of these techniques have been used in the Nankai subduction zone to gain insight into increasing pore pressure and fluid flow, however they do not document spatial variability along the entire borehole length.

Our study is aimed at (a) obtaining a high resolution profile of hydraulic properties and to finely characterise the fault architecture (fault core and damage zone) in the Nankai subduction zone. Identify whether the décollement acts as a significant flow channel. (b) Pore pressure profiles along the accretionary prism, hence assessing the origin of the fluids, especially whether they diffuse from the décollement, or whether they are inherited from sedimentary compaction or from tectonic loading. (c) If the fault is a hydraulic channel, the moderate pressure at shallow depth is compatible with high pressure at moderate depth, which could be associated with the generation of very low-frequency earthquakes (VLFE), episodic tremor and slip (ETS), and slow slip events (SSE) within the Nankai accretionary prism.

To achieve these objectives, we combine drilling engineering methods with geophysical approaches to provide continuous quantitative spatial hydraulic information at meter scale with specific interpretation of the décollement fault zone at the toe of Nankai accretionary prism. We used two independent methods to quantitatively estimate the hydrogeological properties: (i) Direct modeling of fluid flow between the formation and the borehole during drilling from downhole annular pressure (DHAP). (ii) Proxy indicators of pore pressure approaches to support to the fluid flow modeling. The originality of our methodology used a wide range of both logging data (depth-based) and drilling data (time-based).

It's advantageous working with both time and depth because of its ability to relocate each hydraulic anomaly back to a geological framework and to any specific drilling event.

2 GEOLOGICAL SETTING

The Nankai trough is formed by the subduction of the Philippine Sea Plate beneath the Eurasia Plate with the two plates converging at the rate of 41 mm/yr to 65 mm/yr (Seno et al., 1993). The Nankai subduction zone has one of the longest histories of repeated big magnitude earthquakes, spanning around 1,300 years (Ando, 1975). It is an area of high seismic hazard as exemplified by M8+ 1944 Tonankai earthquake and the 1946 Nankaido earthquake (Ando, 1975; Kanamori, 1972) shown in Fig. 1a & b. It has also been identified as a locus of slow slip events (SSE) and very low frequency earthquakes (VLFE) (Araki et al., 2017) with identified predominant frequency of 0.1 Hz near the trench axis of the Nankai Trough (Obara & Ito, 2005).

The Nankai subduction zone has been the focus of the NanTroSEIZE project, which featured 13 expeditions of the Integrated Ocean Drilling Program and International Ocean Discovery Program (both known as IODP). Out of the 13 NanTroSEIZE expeditions, 10 were conducted during the Integrated Ocean Drilling Program that preceded the International Ocean Discovery Program. This program is a coordinated multiexpedition drilling project designed to investigate the mechanics of the fault and the seismogenesis of the Nankai subduction megathrust (Tobin et al., 2020). The main objective of IODP Expedition 358 was to drill and core pass the high amplitude seismic reflector identified as the plate boundary fault zone at site C0002 (Figures 1b). The objective was not achieved due to poor hole conditions, leaving time to drill several contingency holes at Site C0024 (Fig. 1b & c) at the frontal thrust of the accretionary prism to sample and log the hanging wall and decollement zone (Tobin et al., 2020). Site C0024 is located a few kilometers northwest of site C0006 on the frontal anticline that overlies of the frontal thrust (Fig. 1c) and was drilled to a depth of 871 meters below seafloor (mbsf) (Tobin et al., 2020) in 3870 m of seawater column.

Hole C0024A intersected through the décollement at a depth of 813 mbsf, which was interpreted as a complex zone of fault strands and imbrication of thrust slices (Tobin et al., 2020). Cores were obtained in other holes C0024B-C0024E, & G (Fig. 1c) but at shallower intervals, as their drilling was abandoned due to deteriorating borehole conditions at deeper levels (Tobin et al., 2020). The lithological classification is based on core data from Hole C0024B-C0024E, & G with logging unit attributes from Hole C0024A based on relevant measurements of physical properties and information from broadly correlative facies that were previously sampled at nearby sites C0006 and C0007 (Tobin et al., 2020). The lithological units are divided into three with varying thickness and dipping angles: (a) Accretionary trench wedge facies (Unit 1: Subunit 1a, Subunit 1b, Subunit 1c) (b) Upper Shikoku

121 basin hemipelagic-pyroclastic facies (Unit 2: Subunit 2a, Subunit 2b) (c) trench channel complex (unit
122 3).

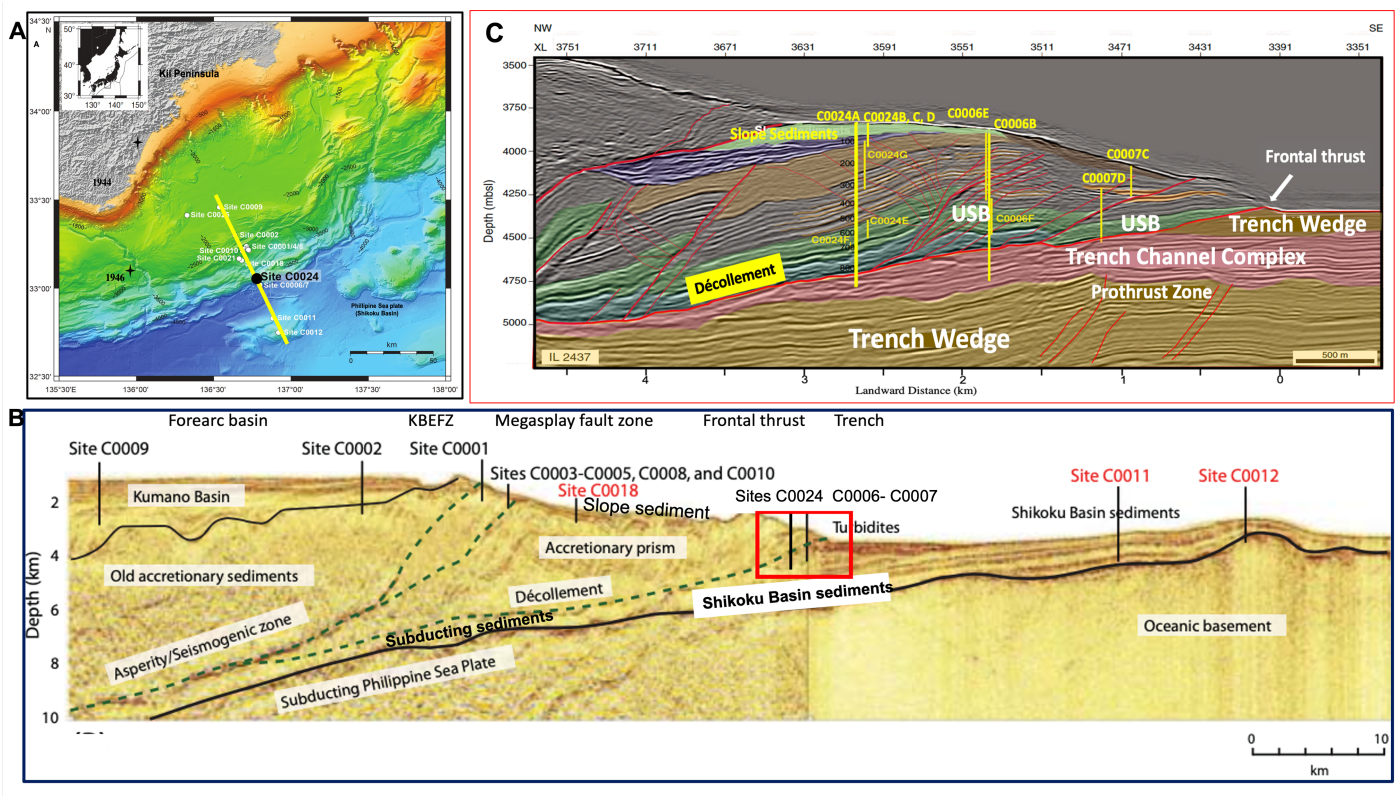

Figure 1. Location of the study site (a) Map of the Nankai subduction zone offshore Japan showing the Kumano transect (modified from Moore et al. (2009)). The transect line is indicated with a thick yellow line. Solid black dots = site C0024, white dots = other NanTroSEIZE sites, black diamond star = location of the two large magnitude earthquakes of 1944 & 1946. (b) Kumano transect line indicated as the yellow line on Fig. 1a showing drill sites of the NanTroSEIZE with few representative faults. Dashed lines = less certain fault locations. KBEFZ = Kumano Basin edge fault zone (modified from Park et al. (2008)). (c) Enlarged location of site C0024 indicated by the red rectangle in Figure 1b. Interpreted seismic depth section of In-line (IL) 2437 in the frontal thrust region with locations of Sites C0024, C0006, and C0007. XL = cross-line. mbsl = meters below sea level, colored shading = seismic stratigraphic packages, red = faults (bold for major faults), yellow = Site C0024, C0006 & C0007 LWD and coring holes, USB =upper Shikoku basin. (Modified from Tobin et al. (2020)).

3 METHODOLOGY

3.1 Overview of drilling, downhole annular pressure (DHAP) measurements and tools

Drilling requires the use of drilling fluids for several reasons: (i) lubricating, cooling, and cleaning the drill bit; (2) controlling formation pressure; and (3) removing and transporting cuttings outside the borehole (Ward & Andreassen, 1997; Hutchinson & Rezmer-Cooper, 1998; Simpson, 2017). Typically, during drilling, the drilling fluid is pumped down through the drill pipe and through the drill bit nozzles (Ward & Andreassen, 1997) (Fig. 2 a). Riserless drilling (Fig. 2a) was used to drill hole C0024A used in this study. The cuttings are pumped out of the borehole with seawater onto the seafloor; hence, nothing is known about the amount of drilling mud or the cuttings that come out of the borehole.

In Hole C0024A, borehole monitoring and data (*in situ* physical rock properties and downhole drilling parameters) were acquired in real time using logging while drilling (LWD) (Arps & Arps, 1964; Tobin et al., 2020). The recorded data are transmitted to operators in real time via drilling mud pulse telemetry or electromagnetic telemetry, or it can be saved in memory, accessed, processed, and interpreted subsequently when the bottom hole assembly (BHA) is recovered from the hole (Fig. 2a, b). These data are measured by specific tools (arcVISION, MicroScope, TeleScope, SonicScope, seismicVISION) that are installed on the BHA (Figure. 2b).

The downhole annular mud pressure (referred hereafter as DHAP) changes were recorded by the arcVISION tool (Fig. 2b). The DHAP sensor is located 7.52 m above the drilling bit with a data sampling rate of 5 seconds, with a resolution of 1 psi (6897 Pa), and maximum annular pressure measurement of 20 kpsi (137.9 MPa) $\pm$ 0.1%. These data are recorded as time series, but are usually converted to depth-based data by the logging operator. In this work, the DHAP (Fig. 2c) and other LWD data like the resistivity, caliper, compressional sonic velocity logs were processed in time and depth.

3.2 DownHole Annular Pressure (DHAP) modeling

Monitoring DHAP during drilling is critical because it helps detect pressure increases caused by fluid influx from the formation into the borehole, or pressure decreases caused by fluid loss circulation into to permeable formations and faults (Hutchinson & Rezmer-Cooper, 1998; Cook et al., 2011; Baggini Almagro et al., 2014; Tobin et al., 2020; Amiri & Doan, 2019). DHAP is made up of two principal components: Static pressure includes the pressure exerted by drilling mud and rock cuttings within the borehole (Fig. 3). Dynamic pressures are cumulative frictional pressure losses within the borehole annulus while drilling (Ward & Andreassen, 1997; Hutchinson & Rezmer-Cooper, 1998). A systematic

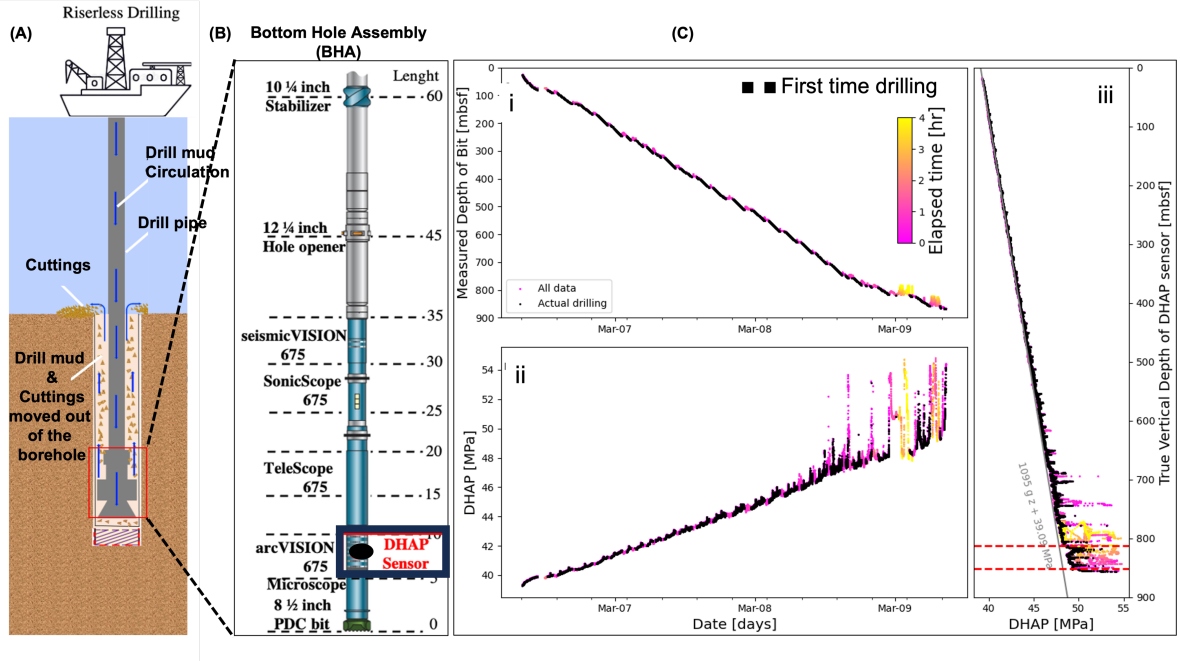

Figure 2. Mud pressure monitoring while drilling hole C0024A (a) A schematic diagram of drilling at Site C0024. The Bottom Hole Assembly (BHA) exhibits a large collection of geophysical tools above the drilling bit b) Zoom on the BHA system used to drill Hole C0024A, with the geophysical tools used for the Logging while drilling (LWD) measurements (Modified from Tobin et al. (2020)). The black rectangle highlights the DownHole Annular Pressure (DHAP) sensor used to record changes in mud pressure during drilling. (c) Time series of drilling data, especially bit depth (part i) and DHAP (part ii). DHAP and bit depth tend to increase with time. Analysis is restricted to DHAP data when each depth was first reached by the drill bit (black data). DHAP increases with the true vertical depth of the DHAP sensor (part iii), with a linear baseline (in gray) corresponding to an equivalent mud density of $1095\ \mathrm{kg/m^3}$. Shaded color: All recorded DHAP data throughout the duration of the drilling. Black data: DHAP data with null elapsed time, i.e. corresponding to the actual drilling, when each depth was first drilled. The location of the 2 strands of the décollement are denoted by horizontal lines.

workflow was used for the DHAP modeling which is designed based on first principles to quantify the inflow along the whole borehole. The workflow is done in two steps: Firstly, we attempt to model the DHAP data considering only the mud circulation along the borehole, related to drilling (modeling of the mud assuming no flow from the formation). This will provide a first fitting of the linear trend of Fig. 2c[iii] but cannot capture all the DHAP anomalies. In a second step, these anomalies will be interpreted as evidence of flow from the formation, to quantify the flow rate entering into the borehole.

3.2.1 Modeling of mud pressure, assuming no flow from the formation

Modeling of DHAP considers the contribution of static pressure and dynamic hydraulic frictional pressure loss induced during pumping by fluid circulation. We assume that swabs and surges are negligible because the interpretation of DHAP is restricted to the data set corresponding to the times corresponding to the actual drilling.

3.2.1.1 Contribution of static effects (including the weight of cuttings)

The density of the returned mud surpasses the density of the mud that was first injected because the mud returning out of the borehole through the annulus conveys rock cuttings (Fig. 3). However, because hole C0024A was drilled with a riserless system, we do not have direct information about the contribution of the cuttings to the drilling mud because it was lost to the seafloor. Therefore, the principle of mass balance is used to estimate the effective density of the returned mud (i.e., the combination of the density of the clean mud and the cuttings). For the sake of this calculation, the following assumptions were made:

(i) Within the borehole is a homogeneous mud with an effective density (ρ_{eff}) assuming the mud is an incompressible fluid and independent of temperature and pressure.

(ii) The volume of mud that returns to the seafloor is equal to the amount of mud that leaves the pumps (i.e., no mud loss , neither storage within the pipes nor annulus).

(iii) For the sake of this first-order estimation, the fluid influx (Q_f) from the formation into/out of the borehole is considered to be minimal in comparison to the pumping flow rate (Q_{pump}).

The mass balance calculation is made on the Eulerian volume system shown in Fig. 3. This volume encompasses the current volume of the borehole (V_{bor}) and the volume $dV = ROP\, dt\, \pi\, \frac{d_b^2}{4}$ of rock to be drilled between the initial drilling time (t_0) and the total drilling time ($t_0 + dt$). The latter volume is controlled by the rate of penetration (ROP) and the borehole diameter (d_b), which is constrained between the nominal bit size and the borehole caliper measured at the time of the passing of the electromagnetic tool, typically several tens of minutes after drilling. We used the caliper values in our calculation to get the upper estimate of the contribution of the cuttings. As flow in and out of the borehole annulus is considered negligible, $Q_{out} \simeq Q_{pump}$ (where Q_{out} is the flow rate out of the borehole), hence the mass balance equation provides an estimate of the effective density (ρ_{eff}) of the mud loaded with cuttings:

$$\rho_{\text{eff}} = \frac{\rho_{MW} Q_{pump} + \rho_r\, ROP\, \pi\, \frac{d_b^2}{4}}{ROP\, \pi\, \frac{d_b^2}{4} + Q_{pump}} \tag{1}$$

Given that the cores could not be recovered for most of the borehole, the bulk density of the formation

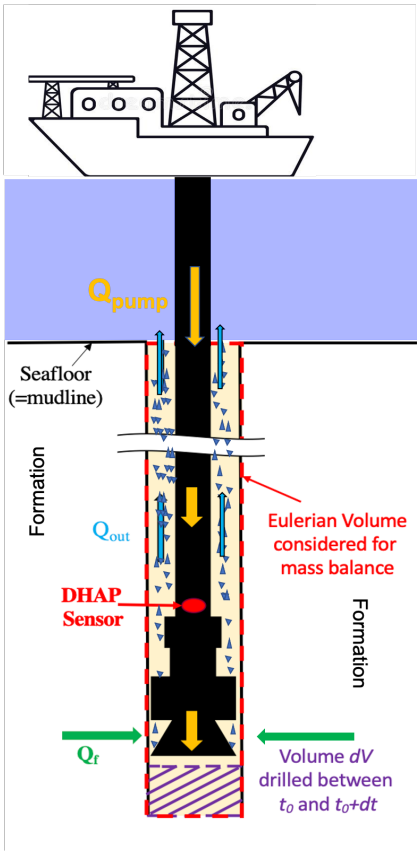

Figure 3. Schematics of the Eulerian system on which mass balance calculation was conducted (delimited by dashed lines around the borehole annulus). The volume drilled between t_0 and $t_0 + dt$ is shown with the diagonal stripes. The arrows show also the fluid flows considered. Both pump flow Q_{pump} and formation flow Q_f (positive in the case of influx to the borehole, negative in the case of outflow) contribute to the flow returning to the surface Q_{out}. The fluid flow into the borehole is assumed to come from a section between the DHAP sensor and the drill bit. Above, an impermeable mud cake is supposed to be fully developed.

was estimated as $\rho_r = \rho_g\,(1-\phi) + \rho_w\phi$, where ρ_g is the grain density determined from the cored section, ρ_w is the density of fluids that fill the pores of the rock (assumed to be seawater, so $\rho_w = 1028\,\mathrm{kg/m^3}$) and ϕ is the porosity of the rock, as estimated on board from Archie's equations using the resistivity logs (Tobin et al., 2020; Bourlange et al., 2003).

3.2.1.2 Contribution of dynamic hydraulic loss

Due to the viscosity of the mud, increased mud pressure at the bottom of the hole is required to allow the mud to flow back to the seafloor via the borehole annulus (Fig. 4). Hydraulic resistance will cause a difference in pressure between the annular pressure at the DHAP sensor position and the seafloor, which depends on the flow circulating up the annulus.

Hydraulic resistance depends on the hydrodynamic regime which is either laminar ($Re \ll 2000$) or turbulent ($Re \gg 4000$) regime. The Reynolds number Re is expressed as:

$$Re = \frac{\rho_{\text{eff}}\, \bar{v}\, d_e}{\mu} \tag{2}$$

where Re is the Reynolds number (dimensionless), ρ_{eff} is the effective density (Eq. 1), μ is the dynamic viscosity of fluid, $\bar{v}$ is the annular average velocity and d_e is the hydraulic diameter (Bourgoyne et al., 1986). The average velocity ($\bar{v}$) is estimated through the mass balance equation, providing a direct relationship with the flow rate out of the borehole (where there is likelihood of fluid exchange between the formation and the borehole (Fig. 3)) and an inverse relationship with the surface area of the drill string:

$$\bar{v} = \frac{4\, Q_{out}}{\pi \left({d_b}^2 - {d_p}^2 \right)} \tag{3}$$

where d_b is the diameter of the borehole (caliper) and d_p is the external diameter of the drill string. The hydraulic diameter (d_e) is defined as the function of d_b and d_p (Bourgoyne et al., 1986):

$$d_e = \sqrt{d_b^2 + d_p^2 - \frac{d_b^2 - d_p^2}{\ln\left(\frac{d_b}{d_p}\right)}} \tag{4}$$

The value of the estimated Reynolds number from Eq. 2 is $Re \gg 50000$. This indicates a turbulent hydrodynamic flow regime exist within the borehole annulus. Hence, the hydraulic frictional pressure loss within the borehole annulus for the interval borehole length (dz) can be determined through the Fanning equation (Bourgoyne et al., 1986):

$$\frac{dp_f}{dz} = \frac{2 f \rho_{\text{eff}} \bar{v}^2}{d_e} \tag{5}$$

where dp_f is the hydraulic pressure loss, f is the Fanning friction coefficient. Blasius (1913) showed that the Fanning friction coefficient (f) is related to the Reynolds number (Bourgoyne et al., 1986):

$$f = \frac{B}{Re^{1/4}} \tag{6}$$

where, experimentally, $B = 0.0791$.

A Newtonian fluid type was assumed for the mud used to drill hole C0024A. Combining equations 5 and 6, we get the appropriate pressure loss equation for a Newtonian fluid turbulence model based on the Fanning equations (Bourgoyne et al., 1986). This equation expresses the gradient of hydraulic pressure loss (dp_f) along a section of the borehole annulus of length (dz):

$$dp_f = 2\, B\, \frac{\rho_{\text{eff}}^{3/4} \bar{v}^{7/4} \mu^{1/4}}{d_e(z)^{5/4}} dz \tag{7}$$

In Eq. 7, it is assumed that the fluid is incompressible and that the flow from the formation does not build up pressure, because it just escapes to the surface through the annulus of the borehole. A new equation is derived to calculate hydraulic pressure loss (dp_f) by combining equations 7, 3, and 4.

This equation is integrated between the seafloor and the current depth of the DHAP sensor to define a forward relationship between dynamic pressure loss (Δp) and flow out of the borehole (Q_{out}).

$$\Delta p(z_{DHAP}) = \frac{4^{9/4}\, B\, Q_{out}^{7/4}}{\pi^{7/4}} F\left(z_{DHAP}\right) = HL\left(Q_{out}\right) \tag{8}$$

Here, $F(z_{DHAP})$ bundles all the depth-dependent terms. For each depth considered, the actual diameter of the borehole as captured by the caliper log (Fig. 6d) and the actual configuration of the drill string (Fig. 2b):

$$F\left(z_{DHAP}\right) = \int_0^{z_{DHAP}} \frac{\rho_{\text{eff}}(z)^{3/4}\, \mu(z)^{1/4}}{\left(d_b\left(z\right)^2 + d_p\left(z\right)^2 - \frac{d_b(z)^2 - d_p(z)^2}{\ln\left(\frac{d_b(z)}{d_p(z)}\right)}\right)^{5/8} \left(d_b\left(z\right)^2 - d_p\left(z\right)^2\right)^{7/4}} dz \tag{9}$$

3.2.2 Estimation of flow between formation and borehole from mud pressure

Any anomaly not captured by the previous forward modeling of DHAP above is attributed to the fluid exchange (Q_f) between the borehole and the surrounding rock formation (Fig. 3). Therefore, we assume that the flow causing the hydraulic loss (Sec. 3.2.1.2) is caused by the total flow $Q_{out} = Q_{pump} + Q_f$. Eq. 8 can be inverted to convert the unexplained DHAP anomaly into an anomaly in the vertical upward flow. Hence, the fluid flow Q_f between the borehole and the formation is given as:

$$Q_f \;=\; HL^{-1}\left(DHAP - \rho_{\text{eff}} g z - P_{sea}\right) \;-\; Q_{pump} \tag{10}$$

where HL is the hydraulic loss function introduced in equation 8, whose fluid parameters were adjusted to fit the baseline of the DHAP profile (Fig. 2c [iii]).

3.3 Pore pressure estimation

Pore pressure modeling was used to support the fluid flow model for self consistency. Pore pressure conditions within the subduction zone are controlled by the permeability and fluid retention capacity of the rock formation, loading history, under-compaction, tectonic or slope change events (Davis et al., 1983; Rubey & Hubbert, 1959; Tobin & Saffer, 2009). The compaction evolution of these sediments in a simple drained diagenetic process supports increase in overburden stress (Terzaghi et al., 1968). Terzaghi & Peck (1948) proposed a relationship between pore fluid pressure, the overburden stress (σ_v) and vertical effective stress (σ_e):

$$\sigma v \;=\; \sigma_e + P_f \tag{11}$$

Where P_f is the pore pressure. Here, the overburden stress (σv) was estimated using the bulk densities derived from the moisture and density (MAD) of the cores obtained from holes C0024 (B, C, D, F,

G) (Fig. 1c), and the porosity data (calculated from Archie's equations using the resistivity log data (Fig. 5a) (see Bourlange et al. (2003) for full description of the methodology).

We used three independent methods to estimate pore pressures as a support to the fluid flow. The first method is derived from consolidation experiments done on rock sampled during the NanTroSEIZE project (Kitajima & Saffer, 2012; Kitajima et al., 2017) and two other methods are Eaton-like methods with empirical parameters derived by the oil and gas industry, each method using a independent dataset (drilling parameters and sonic compressional velocity). These Eaton methods are discussed in the supplementary material.

The first method follows the same workflow as the pore pressure estimation done in Site C0002 (Kitajima et al., 2017). It uses empirical relationships between P-wave velocity, porosity and effective stress derived consolidation experiments performed on samples represent sediments that are about to enter the subduction channel, and hence are not yet tectonically deformed (Kitajima & Saffer, 2012; Kitajima et al., 2017). The samples were coming from Site C0011, cored in the subducting Philippine Sea plate (Fig. 1b).

The first step of the workflow is to derive the porosity from the P-wave velocity data, using the empirical relationship of Erickson & Jarrard (1998):

$$V_p\,[\mathrm{km/s}] \;=1.11\;+\;0.178\,\phi_t+\frac{0.305}{(\phi_t+0.135)^2+0:0775}\;+\;0.61\;(v_{sh}-1)\;X_m \tag{12}$$

where ϕ_t is the total porosity, v_{sh} is the shale volume per unit volume of rock, and X_m accounts for the brutal change in behavior at a critical porosity $\phi_c = 0.39$, above which stress is supported by the fluid rather than by the grain skeleton of the rock (Eq. 13):

$$X_m \;=\; \tanh\left[20\,(\phi_t-\phi_c)\right]-\|\tanh\left[20\,(\phi_t-\phi_c)\right]\| \tag{13}$$

For consistency with the method of Kitajima et al. (2017), we used the porosity inverted from Eq. 12 to compute the void ratio e in the equation below:

$$e \;=\; \frac{\phi}{1-\phi} \tag{14}$$

Void ratio e is the volume of voids relative to the volume of solids, whereas porosity ϕ is the volume of voids relative to the total volume. We assumed a shale volume value of (v_{sh} = 0.66 as in Kitajima et al. (2017).

The second step consists in using experimental relationships between effective stress and the porosity, derived from consolidation experiments by Kitajima & Saffer (2012). Two-end members are considered :

(i) vertical consolidation without horizontal strain (K_0). This loading is similar to the loading occurring during sediment burying in a sedimentary basin. In these conditions, Kitajima & Saffer (2012)

found the following relationships for samples from the Shimano basin, in the Philippine Sea Plate :

$$p' = 10^{\frac{0.89-e}{0.44}} \quad (15)$$

$$q = 0.375 \times p' \quad (16)$$

where p' is the effective mean stress ($p' = \frac{1}{3}(\sigma_1 + \sigma_2 + \sigma_3) - P_f$) and q is the differential stress ($q = \sqrt{\frac{1}{2}\left((\sigma_1 - \sigma_2)^2 + (\sigma_2 - \sigma_3)^2 + (\sigma_3 - \sigma_1)^2\right)}$), where the effective principal stresses (σ_1 is the principal stress direction (further in the manuscript referred to as the overburden stress (σ_v), σ_2 is the principal horizontal stress (further referred to as SH_{max}), σ_3 is the minimum horizontal stress (further referred to as Sh_min)).

(ii) critical state loading (CSL) in which the sample is submitted to a maximum differential stress q.

$$p' = 10^{\frac{0.79-e}{0.40}} \quad (17)$$

$$q = p' \quad (18)$$

With only two equations provided by Eq. 15 or 17, additional assumptions on stress have to be made. A first assumption is that the vertical direction is a principal stress direction and its magnitude is the overburden stresss. Another assumption is about the amplitude of minimum horizontal stress S_{hmin}. Contrary to Kitajima et al. (2017), no leak-off test data is available. Hence, following Zhang & Zhang (2017), we assume the minimum horizontal principal stress is provided by the elastic response to an overburden loading Turcotte & Schubert (2002).

$$S'_{hmin} = S_{hmin} - p_f = (\sigma_v - p_f)\,\frac{\nu}{1-\nu} \quad (19)$$

Poisson's ratio ν was obtained from the V_p and V_s ratio ($\nu = \frac{V_p^2 - V_s^2}{2(V_p^2 - V_s^2)}$). Hence, S_{hmin} could not be retrieved at depths, since V_s data are often not recovered, due to low signal-to-noise ratio. Equations 15 or Equations 17 are inverted to estimate pore pressure p_f and the principal horizontal stress S_{Hmax} in the $K0$ and CSL conditions, respectively.

4 RESULTS

4.1 DHAP modeling: identification of flowing zones within the borehole

We applied the methodology of section 3.2 to the DHAP data of Hole C0024A. The results (Fig. 4b) show the modeling at various steps: (a) with only the clean seawater contribution, (b) with all static contributions, i.e. clean seawater density and cutting weight and (c) with the additional contribution of hydraulic frictional pressure loss associated with mud circulation. The modeling was done for the

entire time series, but the vertical profiles only show the times related to the actual drilling, when the borehole was extended (see Fig. 2c[iii], for a description of the time-depth conversion).

4.1.1 Contribution of cuttings and hydraulic losses on the DHAP

The total calculated effective mud density (mud density + cuttings density using Equation. 1) ranges from $1029.63-1091\ \mathrm{kg/m^3}$. Hence, when compared with the original injected mud density ($1028\ \mathrm{kg/m^3}$) the contribution of rock cuttings density during drilling (equation 1) is estimated to be between $1.63-63\ \mathrm{kg/m^3}$. This results in a maximum of 6.1% percent increase in the effective density value of mud. This suggests that cuttings make a negligible contribution to original injected mud density. The effective density results support the assumptions provided in section 3.2.1.1 for a Eulerian volume system.

Fig. 4 shows the detail results of the DHAP modeling with intermediate outputs (static effects, dynamic effects and mud pressure anomaly) and main output (fluid flow influx). The difference between the full static pressure model (with clean mud and cuttings) and the clean mud model is attributed to the cuttings in Fig. 4b. On Fig. 4b, the static pressure model (clean mud and cuttings) increases slightly above the clean mud pressure, but in a limited way. The parametric investigations (Fig. A1b & c) further show that the difference between the static pressure model and the clean mud pressure is minor, despite modifying the mud property (density and viscosity). The difference remains the same even when the overall mud pressure has increased for the drilling report, as shown in Fig. A1d. Because of its small contribution, the production of cuttings by drilling cannot alone explain the DHAP anomaly of Fig. 4c.

The hydraulic loss along the borehole (equation 8) explains most of the discrepancy between the predicted model and the actual DHAP data (Fig. 4b). The predicted model without flow from the formation fits satisfactorily to the mud pressure (DHAP) data, with a difference less than 1 MPa within the accretionary prism until the décollement zone is reached (Fig. 4c). However, it cannot explain the pressure anomaly (Fig. 4c), up to $2.5-5\ \mathrm{MPa}$ at the décollement interval ($<813\ \mathrm{mbsf}$).

The estimated fluid flux along the borehole based on section 3.2.2 is shown on Fig. 4d. At shallow depths, this flow is negative, meaning mud loss from the borehole to the formation. This is most noticeable between $0-462.8\ \mathrm{mbsf}$ (bottom of lithological subunit 1b) and slightly between $627-700\ \mathrm{mbsf}$. The mud loss is negligible between the depth interval $468.8-570\ \mathrm{mbsf}$, indicating that there is no or negligible flow exchange between the borehole and formation within this depth interval. Our results indicate along the borehole, the interval with the observable large calculated fluid influx into the borehole from the formation is below the décollement to the bottom of borehole. In this interval the influx rate increases to excess of $+0.05\ \mathrm{m^3/s}$ and is most prominent within the two damage zones

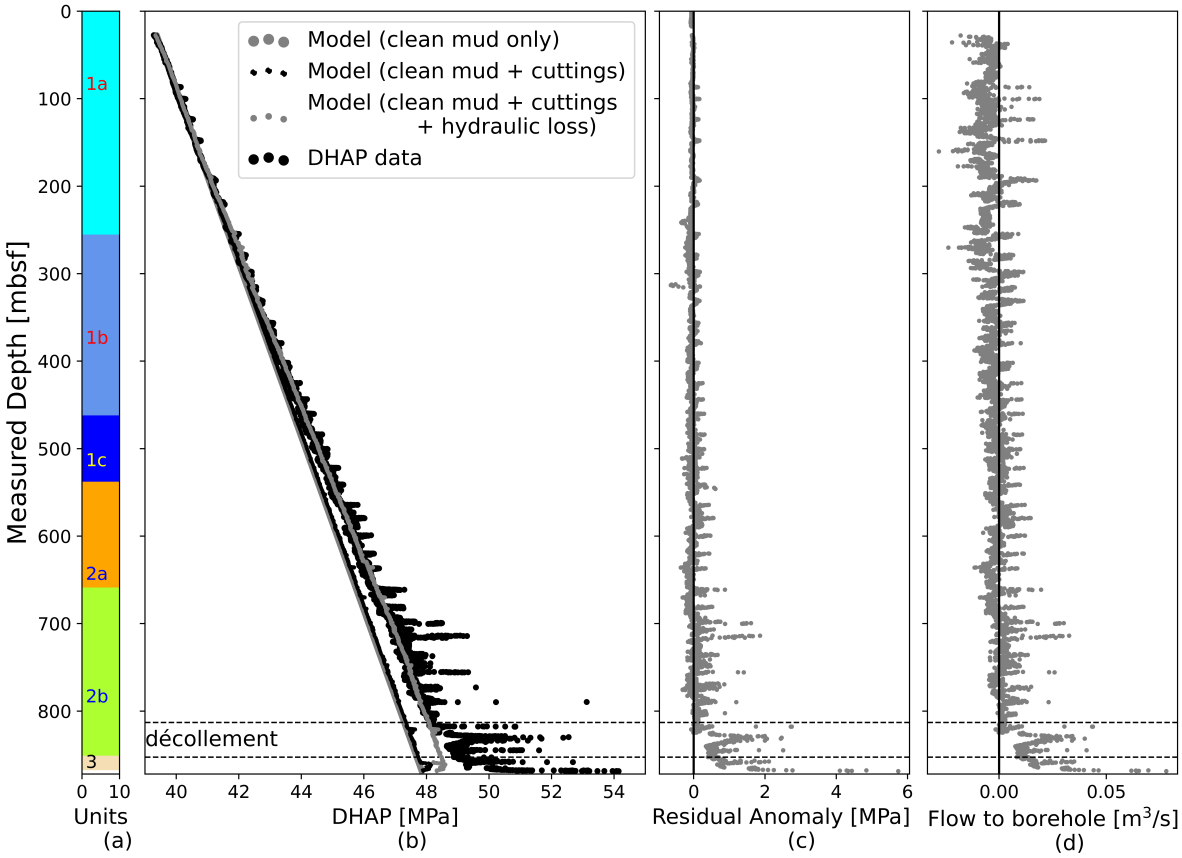

Figure 4. Results derived from the DHAP modeling of hole C0024A. (a) Lithological column (b) Predicted profiles of the mud pressure at various stages of the modeling: with only the contribution of the clean injected drilling fluid (gray (first curve)), with the additional contribution of the weight of the cuttings (dark coloured 2nd curve) and the complete model, with the hydraulic loss of the flowing mud (gray third curve). The DHAP data corresponding to actual drilling times (thick black 4th curve) are well fitted by the latter model, except below the 2 décollement zones (dashed gray horizontal lines). (c) Plot of the difference between the DHAP data (black dots: 4th curve in graph (b)) and the prediction from the full DHAP modeling (gray dots (3rd curve in graph (b)). The null value, where the model exactly fits the data, is highlighted by a thick vertical black line. (d) Flow rate between the formation and the hole. Negative value (to the left of the thick vertical line) corresponds to a flow from the hole to the formation, as expected in normal drilling conditions.

below the two strands of the fault core at a depth of 813 mbsf and 852 mbsf. This large fluid flow (Fig. 4d) into the borehole accounts fully for the significant mud pressure anomaly observed beneath the décollement (Fig. 4c).

4.2 Pore Pressure Prediction Results

Estimated overpressures are indicated as excess pore pressure ($P^* = P_f - P_{hydro}$) above hydrostatic pressures (Yaolin & Chi-Yuen, 1988). The degree to which fluid pressures counteract the total

normal stress generated by the lithostatic load is generally stated in the form of an overpressure ratio ($\lambda = \frac{P_f - P_{seafloor}}{P_{litho} - P_{seafloor}}$) (Rubey & Hubbert, 1959) and the modified excess pore pressure ratio ($\lambda^* = \frac{(P_f - P_{hydro})}{(P_{litho} - P_{hydro})}$) (Davis et al., 1983). The value λ^* normalizes the excess pore pressure relative to the lithostatic pressure (λ^* is 0 at the hydrostatic pore pressure and 1 at the lithostatic), making it easier to assess the importance of the estimated excess pore pressure.

Fig. 5a shows the predicted porosity obtained by inverting Eq. 12, porosity from Archie's law and the MAD. The predicted porosity is in the same range as the porosity predicted from Archie's law from resistivity log and from MAD data acquired onboard during the expedition (Fig. 5a). MAD measure total porosity (connected and unconnected), including those included in potential zeolite deposited with volcanic ashes around 600 mbsf. Electrical resistivity is also sensitive to surface conductivity (Waxman & Smits, 1969; Doan et al., 2011). Hence, local discrepancies are expected. The formulation of Erickson-Jarrard does not account for water-bound resistivity and has been recently revised by Doan et al. (2023). In Fig. 5b, the CSL solution tends to predict large pore pressure all along the borehole, much higher than mud pressure. This contradicts the observation of outflow in the upper section suggested by the DHAP modeling (Fig. 4c). More significantly, such high pore pressure at shallow depths would have impeded drilling and coring. Since Holes C0024B, C0024D, C0024E and C0024G could be drilled with good core recovery down to 320 mbsf, this is not probable.

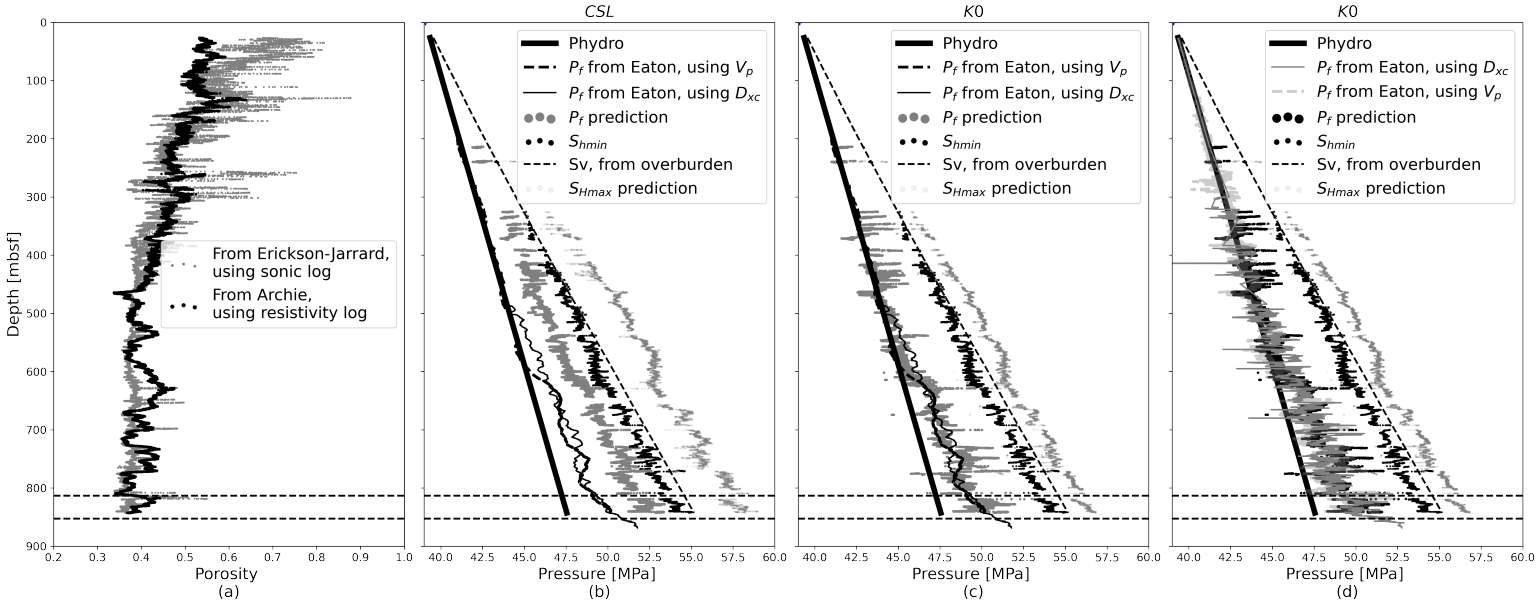

Figure 5. Results from the workflow of Kitajima et al. (2017). (a) Porosity prediction from the inversion of the Erickson-Jarrard equation (Eq. 12) in gray, compared with the porosity derived from Archie's equation applied to the resistivity logs (black) (b) The hydrostatic pressure (thick black first curve), the prediction from Eaton methods are displayed as thick dashed black (2nd curve) and gray (3rd curve), for the version using P-wave velocity and d_{xc} coefficients, respectively. Pore pressure prediction assuming Critical State Loading (CSL) conditions (gray coloured 4th curve to the right). Minimum horizontal stress is the black scatter points (5th curve), lithostatic pressure (6th dashed black curve). The maximum horizontal stress (light gray: 7th curve). (c) Same as in (b) but for K_0 uniaxial loading. The latter pore pressure prediction agrees better with the predictions from Eaton methods. (d) Pore pressure scatter as determined from the raw data. Same as in (c) but for K_0 uniaxial loading. The latter pore pressure prediction agrees better with the predictions from Eaton methods.

Hence, the unixial loading (K_0) end member seems to be more representative of the *in situ* conditions. In particular, the pore pressure prediction agrees with two independent predictions using the Eaton methods (Fig. 5d). The K_0 loading conditions are related to the sedimentary history of the sediments. The congruity of outcomes derived from the multiple approaches indicates that the sediments located at the toe of the accretionary prism have undergone negligible changes as a result of tectonic loading. Consequently, the satisfactory performance of the Eaton equations, despite their reliance on certain underlying assumptions, can be attributed to the minimal impact of these assumptions on the sedimentary conditions being examined.

The pore pressure gradually rises with depth below the depth 510 mbsf (Fig. 5c, d). This point marks the onset of higher pore pressure values over the mud pressure. The highest pore pressure ratio is within the underthrusted sediments not within the accreted sediments above the décollement. There are localized steps in pressure (Fig. 5c & d) when crossing the fault core of the two strands of the décollement at the depth of 813 mbsf and 852 mbsf. The results from the three independent methods averagely varies between $P^* \approx 2.38 - 4.79$ MPa for the excess pore pressure above hydrostatic, the overpressure ratio ($\lambda \approx 0.54 - 0.8$) and the modified excess pore pressure ratio ($\lambda^* \approx 0.28 - 0.62$). The results of pore pressure from the three independent converge reasonably (Fig. 5d). Within the limit of resolution of the methods (about 2MPa, as seen from the scatter of the pressure determined from the raw data), they both overlay and highlight two features: (1) below 500 mbsf, the pore pressure departs from the hydrostat (Fig. 5c & d) and (2) the pore pressure increases again when crossing the first and second strand of the décollement (Fig. 5c & d).

5 DISCUSSION

5.1 Robustness of the estimation of flow modeling and pore pressure

The main result from this study is the determination of a high-resolution profile of the inflow from the formation to the borehole. This profile assumes that at given depths the borehole radius stays constant with time. However, rocks collapsing from the borehole wall along the drillstring could occasionaly block the annulus and create transient peaks in pressure (”packoffs”). To avoid overinterpreting transient peaks, the discussion will be based on the long-term baseline of the flow prediction of Fig. 6i.

Since no other hydraulic data were obtained from the Hole C0024A dataset, like pumping tests or long-term observatories, we assess the relevance of the hydraulic flow profile with 2 methods: (1) self-consistency of behavior of the flow profile and the 3 pore pressure profiles are examined and (2) the consistency of the hydraulic predictions are checked against other independent proxies.

In the top part of the hole, the DHAP analysis predicts that mud fluid enters the formation from the borehole(Fig. 6i & Fig. 4d),within the logging subunit 1a (unconsolidated sediments) and subunit 1b. This loss is consistent with the pore pressure predictions showing that the mud pressure is higher than the formation pore pressure (Fig. 6 j), which is typical of a safe drilling procedure.

The loss of mud pressure to the formation becomes null around 463 mbsf. Consistently, at the same depth, the estimated pore pressure rises and becomes equal to the mud pressure. The flow changes to the right (positive) side of the baseline (Fig. 6i) when the pressure predictions of both Eaton methods converge to a value higher than the mud pressure, around 615 mbsf. This provides a self-consistent picture of the flow. When the mud pressure exceeds the pore pressure, the borehole becomes unstable (Fig. 6d), as seen by the more infrequent peaks in the time series record of mud pressure during non-drilling periods, that is attributed to packoffs (Fig. 2c) . This higher pore pressure in the hemipelagites also explains the difficulties met when coring the C0024F borehole (Fig. 1b), which could not go beyond 731 mbsf (Tobin et al., 2020).

Other geophysical proxies are consistent with a rise in pore pressure below 490 mbsf. The ratio V_P/V_S decreases from that depth (Fig. 6k) also suggesting higher pore pressure. The borehole images (Fig. 6b) also show a change in the breakout direction from that depth, consistent with a change in effective stress that could be related to a non-hydrostatic pore pressure. The large fluid flow predicted at the base of the borehole is consistent with the sharp increase in the real-time temperature of the mud at the base of the hole (Fig. 6l). This is consistent with hot fluids from the formation heating the cold borehole mud injected from the surface. As lithology changes below the second strand of the fault, the Eaton methods cannot be rigorously applied for the lower footwall. However, we would note that the large drop in corrected d-exponent suggests a large increase in pressure below the décollement.

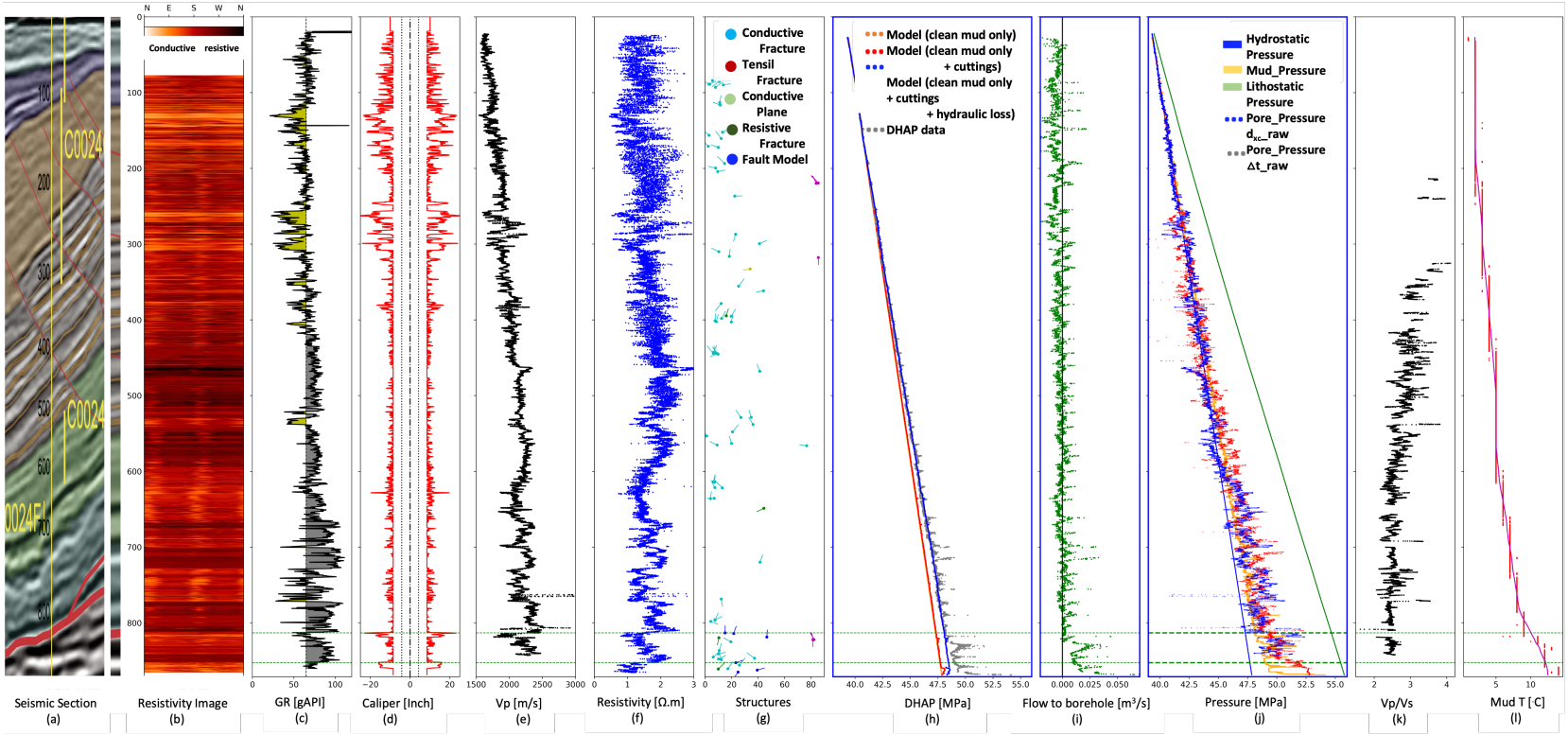

Figure 6. Summary of the properties determined along the whole Hole C0024A. From (a) to (g) are the data already used to identify the lithology and structural properties of the borehole. From (h) to (j) are the new hydraulic data we provide. From (k) to (l) are independent LWD data supporting the hydraulic structure we predict. (a) seismic section (modified from Moore et al. (2009)) (b) Electrical borehole imaging from deep resistivity (c) Gamma-ray (d) caliper log (e) P-wave velocity (f) deep resistivity (g) tadpoles of the main structures picked on the electrical image (h) raw DHAP data, modeled DHAP, effective mud density and tank mud density (i) Fluid flow exchange between formation and the borehole (j) Pore pressure estimated from the 2 Eaton methods, hydrostatic and overburden pressure (k) ratio of P-wave velocity and shear velocity (l) mud fluid temperature.

5.2 Pore pressure increase in the accretionary prism

The results of the pore pressure estimation along the borehole shows that pore pressure increase is not only restricted within the fault zones but also pervasive at deeper depths up to a few hundred meters above the décollement within the accretionary prism. The pore pressure methods converge to an excess of pore pressure in the hemipelagites, suggesting a departure from normal compaction. Either this anomaly existed prior to subduction, or this anomaly is related to the accretion process. IODP Expedition 322 of the NanTroSEIZE project was dedicated to the characterization of subduction inputs, by sampling the sedimentary column entering the accretionary prism at sites C0011 and C0012 (Figure. 1c). From these samples, Hüpers et al. (2015) show an anomalously high porosity zone in the subduction input between the depth of 80-270 mbsf in Hole C0011 and 10-80 mbsf in Hole C0012. This anomaly was explained by the inclusion of volcanic ashes in the sediment, whose silica strengthened the skeleton and prevented further compaction. The volcanic ashes can be identified as highs in gamma-ray logs (Hüpers et al., 2015).

In Hole C0024A, Tobin et al. (2020) identify this anomalous high porosity zone from subduction inputs as a change in porosity at 550 mbsf from electrical logs and from the MAD study from the cores of hole COO24E and related to this zone. This high porosity could affect the sonic log and alter the pore pressure estimation using the Eaton method. This high porosity should also be associated with an increase in permeability and hence with an increase in flow from the borehole to the formation if there were no hydraulic anomalies (change in calculated pore pressure). On the contrary, our analysis of the DHAP shows diminishing flow, and even inflow from the formation below 700 mbsf, which requires the pore pressure to be larger than the mud pressure. Moreover, the high porosity zone is limited in the upper layer of the Shikoku hemipelagics, being 150 m thick in the C0011 hole, while we show that the pore pressure tends to increase steadily with depth over the entire layer of Shikoku hemipelagic clay, even in the zones of low gamma-ray. To summarize, the hydraulic anomaly (fluid flow rate from the formation into the borehole and calculated pore pressure) cannot be discarded as an artefact caused by an original porosity anomaly within the sedimentary column entering the subduction. Although a pre-existing porosity anomaly in the input sediments will affect the occurrence of the hydraulic anomaly, it cannot explain alone the high pressure in the hanging wall.

The accretion of the layers to the prism introduces additional compressional lateral stress onto these formations. In addition, the seismic cross-section of Fig. 1b shows that the slope of the prism evolves with time: a splay fault causes the overthrusting of the landwards sediments onto the layers on which Hole C0024A is drilled, and the deposition of slope sediment on its footwall. Our prediction of pore pressure provides an additional constraint for modeling and understanding of these processes. According to the seismic cross-section of Fig. 1c, Hole C0024A intersects faults at 171 mbsf, 281 mbsf

and 441 mbsf. Since transient peaks in flow rate are not considered in our interpretation, local flow along these faults could not be identified. Crossing these faults does not introduce any large-scale change in pressure, contrary to the décollement. Given that these faults were not identified in the borehole image ((Tobin et al., 2020) and Fig. 6g), these faults can be considered minor, without significant hydraulic influence.

At site C0024, the predicted pore pressure at the toe of accretionary prism along the Kumano transect is higher below the décollement than within the accretionary prism. This is in contrast to the observation made along the Muroto transect farther to the west along the Nankai Trough (Flemings & Saffer, 2018; Gamage & Screaton, 2006) at Sites 808 and 1174 where the predicted pore pressure is higher within the accreted sediments than below the décollement (Flemings & Saffer, 2018; Gamage & Screaton, 2006). This shows different overpressurization states exist in these two transects and could further show variability in the properties of décollement at a regional scale in the Nankai subduction zone.

5.3 Hydraulic structure of the décollement zone

Here, a comparison was made between our new compiled hydraulic information (with a focus at the décollement) and pre-existing information from Tobin et al. (2020). The décollement zone is associated with a fluid flow anomaly zone, with indications of fluid exchange from the formation into the borehole (Fig. 7h). The décollement is complex, with two strands at 813 mbsf and 851 mbsf. Each strand is asymmetric, with a fault core near the hanging wall and damage zones a few meters thick ($6 - 8$m) concentrated in the footwall as observed. Although no core could be recovered from the décollement, the zone was investigated using a complete suite of geophysical logs (Fig. 7 a-f) and the new hydraulic information from this study (highlighted with blue thick edges in Fig. 7g-i).

The asymmetric damage zones are characterised as conductive zones as seen on the electrical borehole imaging from deep resistivity (Fig. 7b), mechanically weak zones as indicated by the larger diameter of the borehole (Fig. 7c), observed steady low P-wave velocity interval (Fig. 7d) and a low deep resistivity (Fig. 7e). The damage zones are marked by the increasing large localized fluid flow (Fig. 7h) which are related to large-scale fractures visible in the image logs (Fig. 7b & f) at 813mbsf and 852mbsf. Due to the large fluid flow and presence of fractures, the permeability of the damage zone is fracture-supported and not matrix-supported.

The fault core was identified as a sharp decrease in resistivity (Fig. 7e) and a larger caliper (Fig. 7c). At the fault core of the décollement, there is no increase in fluid flow at this depth (Figure. 7h). It is also marked with a step in pore pressure (Figure. 7i). The fault core is directly overlain by a hemipelagite hanging wall (Figure. 6c) with lithological characteristics comparable to those of normal

491 cap / seal lithology. It is possible that fine-grained sediments can smear along the fault plane during
492 fault movement, contributing to the low permeability of the fault core.

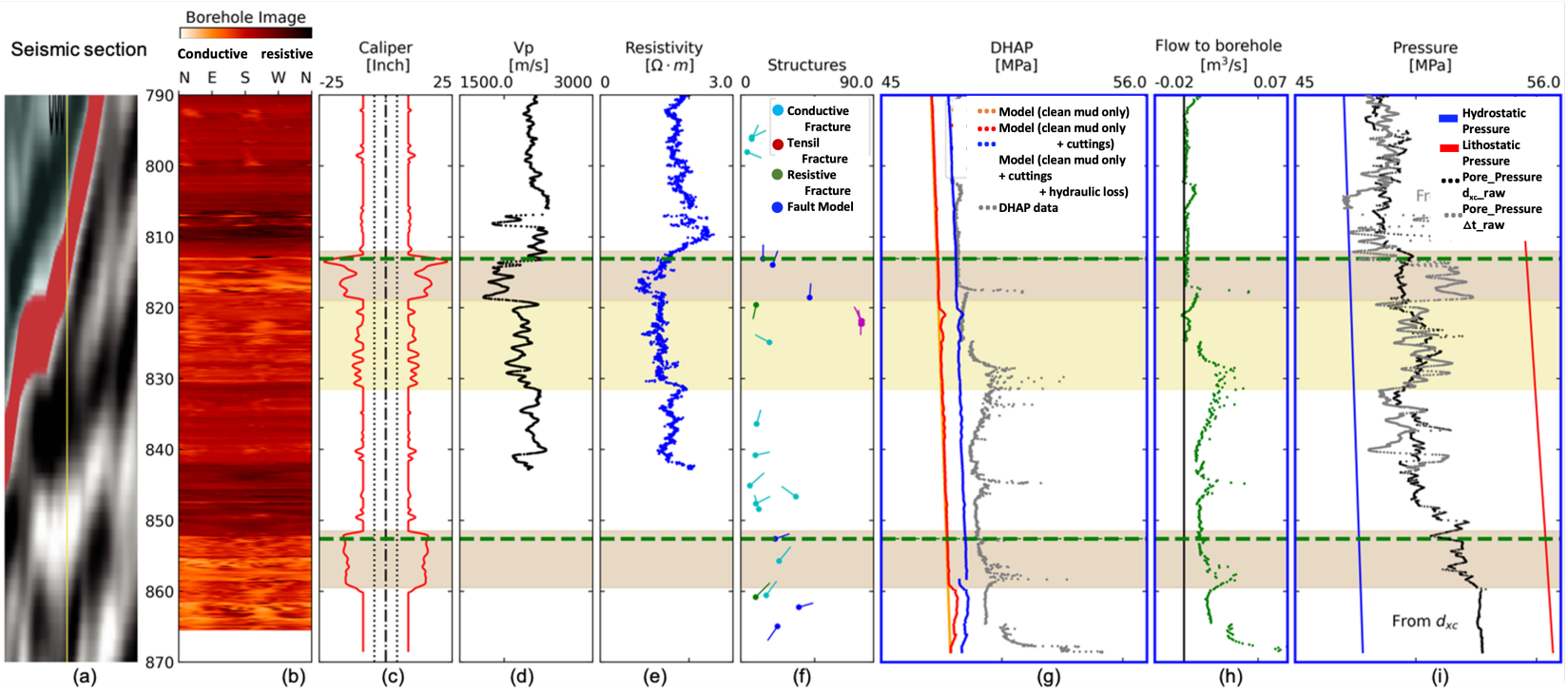

Figure 7. Summary of the hydraulic properties determined along Hole C0024A, with focus on the décollement zone, below 790 mbsf. (a) Seismic section (modified from Moore et al. (2009)) (b) Electrical borehole imaging from deep resistivity (c) caliper log (d) P-wave velocity, (e) deep resistivity, (f) tadpole diagram of the major structures picked on the electrical image (g) raw DHAP data, modeled DHAP, effective mud density and tank mud density (h) fluid flow exchange between the formation and the borehole (i) Pore pressure estimated from the 2 Eaton methods, hydrostatic and overburden pressure.

Along the Kumano transect, our finding shows the property of an impermeable décollement, acting as a barrier to upward fluid convection, which means that there is no hydrological connection between accreted sediments and underthrust below the décollement. The study here examines the toe of the accretionary prism at the Kumano transect; hence the hydrological status may be different in other locations like reported at the Muroto transect (Hirose et al., 2021; Zhang et al., 2021). For example, Zhang et al. (2021) showed that at Sites 1173 & 808, the accreted and underthrust sediments form a single hydrogeological system and that the décollement does not act as a fluid barrier. Our findings are novel, since they are based entirely on data from LWD and MWD tools, which provide hydraulic description of the fault structure at the toe of the accretionary prism.

5.4 Implication of high pore pressure on seismotectonics

The locations of the largest fault slips along subduction megathrust and possible occurrence of devastating tsunami are largely influenced by pore fluid pressure and its variation with depth (Madden et al., 2022). High fluid pressure maintains low effective stress on the fault zone (Rubey & Hubbert, 1959) and also affects the frictional stability of faults and potentially promotes slow earthquakes, as was shown in recent experimental work in Nankai subduction zone (Bedford et al., 2021). In Hole C0024A, fluid flow and high pore pressure are localised on the fault zone, mainly below the décollement (Fig. 7j. Site C0024 is about 3 km away from the trench (Tobin et al., 2020). This has two implications: (1) about the extension toward the trench of the high pore pressure patch below the slope of the Nankai accretionary prism given that site C0024 provides an additional boundary conditions, and (2) about the potential of tsunami generation at the Nankai subduction zone.

Kitajima & Saffer (2012) provided pressure ratios within the low velocity zone under the accretionary slope, but their pore pressure prediction stopped 13 km away from the trench with pore pressure ratio (λ = 0.45-0.91) and modified pore pressure ratio (λ^* = 0.51–0.77). However, recent observations shows that VLFE extends quite shallow (Takemura et al., 2019; Hashimoto et al., 2022), beyond the limits of Kitajima & Saffer (2012). Also Edgington et al. (2021) and Ariyoshi et al. (2021) showed that the SSE of March-May 2020 was shallow enough to induce significant change at the CORK observatory installed in site C0006, which is located 2 km away from the trench (Kinoshita et al., 2018). The high pore pressure seen in site C0024 ($\lambda = 0.54 - 0.8$ & $\lambda^* = 0.28 - 0.62$) suggests that the high pore pressure patch identified by Kitajima & Saffer (2012) could extend almost up to the trench, encompassing the shallow locations of SSE (Edgington et al., 2021; Ariyoshi et al., 2021) and VLFE (Takemura et al., 2019). Diffusion of pore pressure from low velocity zones is possible along the damage zone of the décollement in a up-dip direction (Bourlange & Henry, 2007; Saffer & Tobin, 2011) to the trench. Any earthquake nucleating in the seismogenic zone might propagate in an up-dip

direction, inducing large slip at the trench, since the stress change necessary to produce slip is reduced when effective normal stress is lower..

The hydraulic state of the décollement found along the Kumano transect differs from the Muroto transect, 150 km to the West, with slightly lower pore pressure ratio ($\lambda = 0.71$) , but with a different distribution of pore pressure (Flemings & Saffer, 2018; Zhang et al., 2021). In the Muroto transect, it is the hanging wall that is more overpressurized, than the footwall (Flemings & Saffer, 2018; Zhang et al., 2021). Hence the incoming sediments may be less pressurised, inducing reduced pore pressure downdip. Takemura et al. (2019) has shown there are more SSE and VLFE occurrence along the Kumano transect than in the Muroto transect. This hints that the differences in hydraulic structures at the toe of the accretionary prism reflect different pore pressure distribution downdip, and different seismotectonic behavior along the subduction transect.

6 CONCLUSION

In this study, a new methodology was developed to characterize the hydraulic state along the C0024A borehole, by processing both drilling and geophysical data, in both time and space. The results provide a self-consistent description of the fluid flow and pore pressure profile along the hole. High pore pressure occurs in a large part of the accretionary prism and is not only restricted only to the fault zone. The décollement fault zone is associated with a hydraulic anomaly with a large fluid flow and high pore pressure.

Our consistent results have further shown that the toe of the accretionary prism is characterized by high pore pressure, that could favor the occurrence of SSE and tsunamigenic earthquakes. This study helps characterizing the hydromechanical state of a plate boundary and refining the potential of the décollement to be the locus of devastating tsunamigenic earthquakes. This study is a first step to understanding the full hydraulics of the Nankai subduction zone. Since several other riserless holes were drilled during the NanTroSEIZE campaigns with similar time series of LWD annular pressure data, our methodology can be replicated there for an even fuller understanding.

ACKNOWLEDGMENTS

Special appreciation to the staff onboard Chikyu drilling vessel for their expertise and their kindness. MLD also thanks David Castillo for discussion on the processing of drilling data, both in time and space. We thank the Petroleum Technology Development Fund (PTDF) Nigeria, for funding the PhD research.

DATA AVAILABILITY

The input files and Jupyter notebooks are accessible at the Zenodo data repository: `https://doi.org/10.5281/zenodo.6909792`

References

Amiri, H. & Doan, M.-L., 2019. Hydrological features across the Japan Trench , derived from pressure while drilling of expedition IODP 343 (J-FAST), in *American Geophysical Union, Fall Meeting*, pp. T51G–0377.

Ando, M., 1975. Source mechanisms and tectonic significance of historical earthquakes along the nankai trough, japan, *Tectonophysics*, **27**, 119–110.

Araki, E., Saffer, D. M., Kopf, A. J., Wallace, L. M., Kimura, T., Machida, Y., Ide, S., & Davis, E., 2017. Recurring and triggered slow-slip events near the trench at the Nankai Trough subduction megathrust, *Science*, **356**(6343), 1157–1160.

Ariyoshi, K., Kimura, T., Miyazawa, Y., Varlamov, S., Iinuma, T., Nagano, A., Gomberg, J., Araki, E., Miyama, T., Sueki, K., Yada, S., Hori, T., Takahashi, N., & Kodaira, S., 2021. Precise monitoring of pore pressure at boreholes around nankai trough toward early detecting crustal deformation, *Frontiers in Earth Science*, **9**.

Arps, J. & Arps, J., 1964. The Subsurface Telemetry Problem-A Practical Solution, *Journal of Petroleum Technology*, **16**(05), 487–493.

Baggini Almagro, S. P., Frates, C., Garand, J., & Meyer, A., 2014. Sealing fractures: Advances in lost circulation control treatments, *Oilfield Review*, **26**(3), 4–13.

Becker, K. & Davis, E., 2005. A review of CORK designs and operations during the Ocean Drilling Program, *Proceedings of the IODP, 301*, **301**.

Bedford, J. D., Faulkner, D. R., Allen, M. J., & Hirose, T., 2021. The stabilizing effect of high pore-fluid pressure along subduction megathrust faults: Evidence from friction experiments on accretionary sediments from the nankai trough, *Earth and Planetary Science Letters*, **574**, 117161.

Bekins, B. A., Matmon, D., Screaton, E. J., & Brown, K. M., 2011. Reanalysis of in situ permeability measurements in the Barbados décollement, *Geofluids*, **11**(1), 57–70.

Bingham, M. G., 1965. *A new approach to interpreting rock drillability*, Petroleum Pub. Co.

Blasius, H., 1913. *Das Ähnlichkeitsgesetz bei Reibungsvorgängen in Flüssigkeiten*, Springer, Berlin Heidelberg.

Bourgoyne, A. T., Millheim, K. K., Chenevert, M. E., & Young, F. S., 1986. *Applied Drilling Engineering*, Society of Petroleum Engineers.

588 Bourlange, S. & Henry, P., 2007. Numerical model of fluid pressure solitary wave propagation along
589 the décollement of an accretionary wedge: Application to the nankai wedge, *Geofluids*, **7**, 323–334.
590 Bourlange, S., Henry, P., Moore, C., Mikada, H., & Klaus, A., 2003. Fracture porosity in the
591 décollement zone of nankai accretionary wedge using logging while drilling resistivity data, *Earth*
592 *and Planetary Science Letters*, **209**, 103–112.
593 Bowers, G., 1995. Pore pressure estimation from velocity data : Accounting for overpressure mech-
594 anisms besides undercompaction, *Society of petroleum engineers*, **SPE 27488**(June), 89–95.
595 Caine, J. S., Evans, J. P., & Forster, C. B., 1996. Fault zone architecture and permeability structure,
596 *Geology*.
597 Chester, F. M., Evans, J. P., & Biegel, R. L., 1993. Internal structure and weakening mechanisms of
598 the San Andreas Fault, *Journal of Geophysical Research*, **98**(B1), 771–786.
599 Cook, J., Growcock, F., Guo, Q., Hodder, M., & Van Oort, E., 2011. Stabilizing the wellbore to
600 prevent lost circulation, *Oilfield Review*, **23**(4), 26–35.
601 Daigle, H. & Piña, O., 2016. Data report: permeability, consolidation properties, and grain size
602 of sediments from Sites U1420 and U1421, offshore southern Alaska, *Proceedings of the Ocean*
603 *Drilling Program*, **341**.
604 Davis, D., Suppe, J., & Dahlen, F. A., 1983. Mechanics of fold-and- thrust belts and accretionary
605 wedges., *Journal of Geophysical Research*, **88**(B2), 1153–1172.
606 Davis, E. & Becker, K., 1994. Formation Temperatures and Pressures in a Sedimented Rift Hy-
607 drothermal System: 10 Months of CORK Observations, Holes 857D and 858G, *Proceedings of the*
608 *Ocean Drilling Program, 139 Scientific Results*, **139**, 649–666.
609 Doan, M.-L., Brodsky, E. E., Kano, Y., & Ma, K.-F., 2006. In situ measurement of the hydraulic
610 diffusivity of the active Chelunepu Fault, Taiwan, *Geophysical Research Letters*, **33**(16).
611 Doan, M. L., Conin, M., Henry, P., Wiersberg, T., Boutt, D., Buchs, D., Saffer, D., McNeill, L. C.,
612 Cukur, D., & Lin, W., 2011. Quantification of free gas in the Kumano fore-arc basin detected from
613 borehole physical properties: IODP NanTroSEIZE drilling Site C0009, *Geochemistry, Geophysics,*
614 *Geosystems*, **12**(1).
615 Doan, M.-L., Dutilleul, J., & Henry, P., 2023. Effective porosity profile at iodp site c0002 in the heart
616 of the nankai accretionary prism, and its use for predicting in situ seismic velocities, *Geophysical*
617 *Research Letters*, **50**(4), e2022GL100209, e2022GL100209 2022GL100209.
618 Eaton, B. A., 1972. The effect of overburden stress on geopressure prediction from well logs, *Journal*
619 *of Petroleum Technology*, **24**(08), 929–934.
620 Edgington, J., Williams, C., & Saffer, D., 2021. Migration of Shallow Slow Slip Events to Trench:
621 Evidence from borehole observatories in the Nankai Trough, in *AGU Fall Meeting Abstracts*, vol.

2021, pp. T25C–0188.

Erickson, S. N. & Jarrard, R. D., 1998. Velocity-porosity relationships for water-saturated siliciclastic sediments, *Journal of Geophysical Research*, **103**(B12), 30385–30406.

Faulkner, D. R., Jackson, C. A., Lunn, R. J., Schlische, R. W., Shipton, Z. K., Wibberley, C. A., & Withjack, M. O., 2010. A review of recent developments concerning the structure, mechanics and fluid flow properties of fault zones, *Journal of Structural Geology*, **32**, 1557–1575.

Fisher, A., Wheat, C., Becker, K., Cowen, J., Orcutt, B., Hulme, S., Inderbitzen, K., Haddad, A., Pettigrew, T., Davis, E., Jannasch, H., Grigar, K., Aduddell, R., Meldrum, R., Macdonald, R., & Edwards, K., 2011. Design, deployment, and status of borehole observatory systems used for single-hole and cross-hole experiments, IODP Expedition 327, eastern flank of Juan de Fuca Ridge, *Proceedings of the Ocean Drilling Program*, **327**.

Flemings, P. B. & Saffer, D. M., 2018. Pressure and Stress Prediction in the Nankai Accretionary Prism: A Critical State Soil Mechanics Porosity-Based Approach, *Journal of Geophysical Research: Solid Earth*, **123**(2), 1089–1115.

Gamage, K. & Screaton, E., 2006. Characterization of excess pore pressures at the toe of the Nankai accretionary complex, Ocean Drilling Program sites 1173, 1174, and 808: Results of one-dimensional modeling, *Journal of Geophysical Research: Solid Earth*, **111**(4), 1–13.

Gearhart, M., Ziemer, K. A., & Knight, O. M., 1981. Mud Pulse MWD Systems Report, *Journal of Petroleum Technology*, **33**(12), 2301–2306.

Hammerschmidt, S., Davis, E. E., & Kopf, A., 2013. Fluid pressure and temperature transients detected at the Nankai Trough Megasplay Fault: Results from the SmartPlug borehole observatory, *Tectonophysics*, **600**, 116–133.

Hashimoto, Y., Sato, S., Kimura, G., Kinoshita, M., Miyakawa, A., Moore, G. F., Nakano, M., Shiraishi, K., & Yamada, Y., 2022. Décollement geometry controls on shallow very low frequency earthquakes, *Scientific Reports*, **12**(1), 1–9.

Henry, P., 2000. Fluid flow at the toe of the Barbados accretionary wedge constrained by thermal, chemical, and hydrogeologic observations and models, *Journal of Geophysical Research: Solid Earth*, **105**(B11), 25855–25872.

Hirose, T., Hamada, Y., Tanikawa, W., Kamiya, N., Yamamoto, Y., Tsuji, T., Kinoshita, M., Heuer, V. B., Inagaki, F., Morono, Y., & Kubo, Y., 2021. High fluid-pressure patches beneath the décollement: A potential source of slow earthquakes in the nankai trough off cape muroto, *Journal of Geophysical Research: Solid Earth*, **126**(6), e2021JB021831.

Hüpers, A., Ikari, M. J., Dugan, B., Underwood, M. B., & Kopf, A. J., 2015. Origin of a zone of anomalously high porosity in the subduction inputs to Nankai Trough, *Marine Geology*, **361**,

147–162.

Hutchinson, M. & Rezmer-Cooper, L., 1998. Using downhole annular pressure measurements to anticipate drilling problems, *Proceedings - SPE Annual Technical Conference and Exhibition*, **1999-September**, 535–549.

Jaeger, J. C., 1971. Friction of Rocks and Stability of Rock Slopes, *Geotechnique*, **21**(2), 97–134.

Jannasch, H. W., Davis, E. E., Kastner, M., Morris, J. D., Pettigrew, T. L., Plant, J. N., Solomon, E. A., Villinger, H. W., & Wheat, C. G., 2003. CORK-II: Long-Term Monitoring of Fluid Chemistry, Fluxes, and Hydrology in Instrumented Boreholes at the Costa Rica Subduction Zone, *Proceedings of the Ocean Drilling Program, 205 Initial Reports*, **205**, 1–36.

Jorden, J. R. & Shirley, O. J., 1966. Application of drilling performance data to overpressure detection, *Journal of Petroleum Technology*, (49), 1387–1394.

Kanamori, H., 1972. Tectonic implications of the 1943 Tonankai and the 1946 Nankaido earthquakes, *Phys. Earth Planet. Inter.*, **5**, 129–139.

Kastner, M., Becker, K., Davis, E. E., Fisher, A. T., Jannasch, H. W., Solomon, E. A., & Wheat, G., 2006. New insights into the hydrogeology of the oceanic crust: Through long-term monitoring, *Oceanography*, **19**(SPL.ISS. 4), 46–57.

Kinoshita, C., Saffer, D., Kopf, A., Roesner, A., Wallace, L. M., Araki, E., Kimura, T., Machida, Y., Kobayashi, R., Davis, E., Toczko, S., & Carr, S., 2018. Changes in Physical Properties of the Nankai Trough Megasplay Fault Induced by Earthquakes, Detected by Continuous Pressure Monitoring, *Journal of Geophysical Research: Solid Earth*, **123**(2), 1072–1088.

Kitajima, H. & Saffer, D. M., 2012. Elevated pore pressure and anomalously low stress in regions of low frequency earthquakes along the Nankai Trough subduction megathrust, *Geophysical Research Letters*, **39**(23), 1–5.

Kitajima, H., Saffer, D., Sone, H., Tobin, H., & Hirose, T., 2017. In Situ Stress and Pore Pressure in the Deep Interior of the Nankai Accretionary Prism, Integrated Ocean Drilling Program Site C0002, *Geophysical Research Letters*, **44**(19), 9644–9652.

Madden, E. H., Ulrich, T., & Gabriel, A.-A., 2022. The state of pore fluid pressure and 3-d megathrust earthquake dynamics, *Journal of Geophysical Research: Solid Earth*, **127**.

Miller, S. A., 2013. The Role of Fluids in Tectonic and Earthquake Processes, in *Advances in Geophysics*, vol. 54, chap. 1, pp. 1–46, Elsevier Inc.

Moore, G., Park, J., Bangs, N., Gulick, S., Tobin, H., Nakamura, Y., Saito, S., Tsuji, T., Yoro, T., Tanaka, H., Uraki, S., Kido, Y., Sanada, Y., Kuramoto, S., & Taira, A., 2009. Structural and seismic stratigraphic framework of the NanTroSEIZE Stage 1 transect, *Proceedings of the Ocean Drilling Program*, **314**.

690 Obara, K. & Ito, Y., 2005. Very low frequency earthquakes excited by the 2004 off Kii peninsula
691 earthquakes: A dynamic deformation process in the large accretionary prism, *Earth, Planets and*
692 *Space*, **57**(4), 321–326.
693 Park, J.-O., Tsuru, T., No, T., Takizawa, K., Sato, S., & Kaneda, Y., 2008. A high-resolution 3d seis-
694 mic reflection survey and prestack depth imaging in the nankai trough off southeast kii peninsula, ,
695 **61**(3), 231–241.
696 Rehm, B. & McClendon, R., 1971. Measurement of formation pressure from drilling data, *SPE*
697 *Annual Technical Conference and Exhibition*, SPE-3601-MS.
698 Rowe, K. T., Screaton, E. J., & Ge, S., 2012. Coupled fluid flow and deformation modeling of
699 the frontal thrust region of the Kumano Basin transect, Japan: Implications for fluid pressures and
700 decollement downstepping, *Geochemistry, Geophysics, Geosystems*, **13**(1), 1–18.
701 Rubey, W. W. & Hubbert, M. K., 1959. Role of fluid pressure in mechanics of overthrust faulting:
702 II. Overthrust belt in geosynclinal area of western Wyoming in light of fluid-pressure hypothesis,
703 *Bulletin of the Geological Society of America*, **70**(2), 167–206.
704 Saffer, D. M. & Tobin, H. J., 2011. Hydrogeology and Mechanics of Subduction Zone Forearcs:
705 Fluid Flow and Pore Pressure, *Annual Review of Earth and Planetary Sciences*, **39**(1), 157–186.
706 Sawyer, A. H., Flemings, P., Elsworth, D., & Kinoshita, M., 2008. Response of submarine hydrologic
707 monitoring instruments to formation pressure changes: Theory and application to Nankai advanced
708 CORKs, *Journal of Geophysical Research: Solid Earth*, **113**(1), 1–16.
709 Screaton, E. & Ge, S., 1997. An assessment of along-strike fluid and heat transport within the
710 Barbados Ridge accretionary complex: Results of preliminary modeling, *Geophysical Research*
711 *Letters*, **24**(23), 3085–3088.
712 Seno, T., Stein, S., & Gripp, A. E., 1993. A model for the motion of the philippine sea plate consistent
713 with nuvel-1 and geological data, *Journal of Geophysical Research*, **98**.
714 Shi, Y. & Wang, C.-Y., 1985. High pore pressure generation in sediments in front of the Barbados
715 Ridge Complex, *Geophysical Research Letters*, **12**(11), 773–776.
716 Simpson, D. A., 2017. *Well-Bore Construction (Drilling and Completions)*.
717 Skarbek, R. M. & Saffer, D. M., 2009. Pore pressure development beneath the décollement at the
718 Nankai subduction zone: Implications for plate boundary fault strength and sediment dewatering,
719 *Journal of Geophysical Research: Solid Earth*, **114**(7), 1–20.
720 Spinelli, G. A., Saffer, D. M., & Underwood, M. B., 2006. Hydrogeologic responses to three-
721 dimensional temperature variability, Costa Rica subduction margin, *Journal of Geophysical Re-*
722 *search: Solid Earth*, **111**(4), 1–15.
723 Takemura, S., Matsuzawa, T., Noda, A., Tonegawa, T., Asano, Y., Kimura, T., & Shiomi, K., 2019.

724 Structural Characteristics of the Nankai Trough Shallow Plate Boundary Inferred From Shallow
725 Very Low Frequency Earthquakes, *Geophysical Research Letters*, **46**(8), 4192–4201.
726 Terzaghi, K. & Peck, R. B., 1948. *Soil Mechanics in Engineering Practice*, John wiley & sons, 1st
727 edn.
728 Terzaghi, K., Peck, R. B., & Mesri, G., 1968. *Soil Mechanics in Engineering Practice*, Wiley, 3rd
729 edn.
730 Tobin, H. & Saffer, D., 2009. Elevated fluid pressure and extreme mechanical weakness of a plate
731 boundary thrust, Nankai Trough subduction zone, *Geology*, **37**(8), 679–682.
732 Tobin, H., Hirose, T., Ikari, M., Kanagawa, K., Kimura, G., Kinoshita, M., Kitajima, H., Saffer,
733 D., Yamaguchi, A., Eguchi, N., Maeda, L., Toczko, S., Bedford, J., Chiyonobu, S., Colson, T.,
734 Conin, M., Cornard, P., Dielforder, A., Doan, M., Dutilleul, J., Faulkner, D., Fukuchi, R., Guérin,
735 G., Hamada, Y., Hamahashi, M., Hong, W., Ijiri, A., Jaeger, D., Jeppson, T., Jin, Z., John, B.,
736 Kitamura, M., Kopf, A., Masuda, H., Matsuoka, A., Moore, G., Otsubo, M., Regalla, C., Sakaguchi,
737 A., Sample, J., Schleicher, A., Sone, H., Stanislowski, K., Strasser, M., Toki, T., Tsuji, T., Ujiie, K.,
738 Underwood, M., Yabe, S., Yamamoto, Y., Zhang, J., Sanada, Y., Kido, Y., Ber, E. L., & Saito,
739 S., 2020. Expedition 358 summary, in *Volume 358: NanTroSEIZE Plate Boundary Deep Riser 4:*
740 *Nankai Seismogenic/Slow Slip Megathrust*, International Ocean Discovery Program.
741 Tsuji, T., Tokuyama, H., Costa Pisani, P., & Moore, G., 2008. Effective stress and pore pressure in the
742 Nankai accretionary prism off the Muroto Peninsula, southwestern Japan, *Journal of Geophysical*
743 *Research: Solid Earth*, **113**(11), 1–19.
744 Turcotte, D. L. & Schubert, G., 2002. *Geodynamics*, Cambridge University Press, 2nd edn.
745 Ward, C. D. & Andreassen, E., 1997. Pressure while drilling data improves reservoir drilling perfor-
746 mance, *Proceedings of the Drilling Conference*, pp. 159–168.
747 Waxman, M. H. & Smits, L. J. M., 1969. Electrical conductivities in oil-bearing shaly sand, *SPE*
748 *Journal.*, **8**(2), 107–122.
749 Wheat, C. G., Jannasch, H. W., Fisher, A. T., Becker, K., Sharkey, J., & Hulme, S., 2010. Sub-
750 seafloor seawater-basalt-microbe reactions: Continuous sampling of borehole fluids in a ridge flank
751 environment, *Geochemistry, Geophysics, Geosystems*, **11**(7), 1–18.
752 Yaolin, S. & Chi-Yuen, W., 1988. Generation of high pore pressures in accretionary prisms: infer-
753 ences from the Barbados Subduction Complex, *Journal of Geophysical Research*, **93**(B8), 8893–
754 8910.
755 Zhang, J. & Yin, S., 2017. Real-time pore pressure detection: Indicators and improved methods,
756 *Geofluids*, (1).
757 Zhang, J., Hüpers, A., Kreiter, S., & Kopf, A. J., 2021. Pore Pressure Regime and Fluid Flow

Processes in the Shallow Nankai Trough Subduction Zone Based on Experimental and Modeling Results from IODP Site C0023, *Journal of Geophysical Research: Solid Earth*, **126**(2), 1–19.

Zhang, Y. & Zhang, J., 2017. Lithology-dependent minimum horizontal stress and in-situ stress estimate, *Tectonophysics*, **703-704**, 1–8.

This paper has been produced using the Blackwell Scientific Publications GJI LaTeX2e class file.

Table 1. List of symbols and notation

Symbol or acronym	Meaning
ϕ	Porosity of the rock formation (pu)
μ	Dynamic viscosity of the mud ($\mathrm{Pa \cdot s}$)
ρ_{eff}	Effective density of the mud, cuttings included ($\mathrm{kg/m^3}$)
ρ_g	Density of the rock matrix (=grain density ($\mathrm{kg/m^3}$))
ρ_{MW}	"Mud Weight", i.e. density of the clean mud, free of cuttings ($\mathrm{kg/m^3}$)
ρ_r	rock formation density ($\mathrm{kg/m^3}$)
ρ_w	Density of the fluid filling the pores of the rock , assumed to be seawater ($\mathrm{kg/m^3}$)
σ_e	Effective stress (Pa)
σ_v	Total overburden stress (Pa)
σ_{vg}	Overburden gradient (Pa)
B	Blasius cofficient (dimensionless)
BHA	BottomHole Assembly (equipment at the base of the drill string)
c	Compaction parameter
d_b	Diameter of the borehole (= caliper) (m)
d_p	Diameter of the drill string (pipe or BHA, depending on depth considered) (m)
dp_f	hydraulic pressure loss (Pa)
d_x	d-exponent
d_{xc}	Corrected d-exponent
HL	Function relating hydraulic loss to flow rate (Eq. 8)
mbsf	Meters below seafloor (m)
P_f	Pore fluid pressure (Pa)
P_{hg}	Hydrostatic pressure gradient (Pa)
P_{sea}	Seawater Pressure at the seafloor or mudline (Fig. 3 (Pa))
Q_f	Additional flow from the formation (m^3/s)
Q_{out}	Total flow rate flowing upwards in the annulus above DHAP sensor (Figure.. 3)(m^3/s)
Q_{pump}	Flow rate of clean mud pumped into the borehole (m^3/s)
Re	Reynolds number (dimensionless)
$\bar{v}$	Average mud velocity within the borehole annulus (m/s)
Z	True Vertical Depth (TVD)(m)

APPENDIX A: SUPPLEMENTARY MATERIAL

A1 Logging tools

Logging while drilling (LWD) allows real-time monitoring of the borehole *in situ* physical rock qualities (lithological, fluid, pressure and structural properties) and the drilling parameters. Data are recorded and transmitted to operators in real time via drilling mud pulse telemetry or electromagnetic telemetry (Gearhart et al., 1981). Alternatively, data can be saved in memory, accessed, processed and interpreted in the future when the bottom hole assembly (BHA) is recovered from the hole (Gearhart et al., 1981). For hole C0024A the following sensors (arcVISION, MicroScope, TeleScope, SonicScope, and seismicVISION) were used for recording subsurface informations (See Appendix A1) (Tobin et al., 2020). The LWD tools provide a time series of drill bit location and data from the geophysical sensors. Therefore, it becomes important to process these data and extract the first time that the drill bit reached every depth.

Table A1. MWD/LWD tools, Expedition 358. MWD = measurement while drilling, LWD = logging while drilling (modified from Tobin et al. (2020))

MWD/LWD	Measured data and units	Total Sensor length Distance from bit (m)
MicroScope 675	Natural gamma ray (gAPI), galvanic resistivity (Ωm), resistivity image, caliper (in)	5.89
arcVISION 675	DHAP (MPa), temperature (°C) resistivity(Ωm), gamma ray (gAPI),	11.56
TeleScope 675	Natural gamma ray (gAPI), torque (kNm), downhole weight on bit (kN), rate of penetration (m)	19.99
SonicScope 675	V_p (μs/ft), V_s (μs/ft)	29.99
seismicVISION 675	Seismic velocity, time-depth relationship, corridor stack	34.48

A2 Parametric study of mud pressure modeling without flow from the formation

Viscosity of the mud used for drilling the borehole is a key parameter in the Equations. 9 for calculating the hydrualic pressure loss. A service company onboard made systematic rheological measurements of the mud prepared for drilling. This tank mud is thixotropic, with a viscosity that varies between $2 \times 10^{-3}\,\mathrm{Pa \cdot s}$ and $52 \times 10^{-3}\,\mathrm{Pa \cdot s}$. However, there is inconsistency between the official injected mud density and the effective mud density determined from actual DHAP data. Due to this uncertainty about the actual composition of the borehole fluid, we first forward-estimated the hydrodynamic contribution assuming the fluid had purely Newtonian viscosity and testing a wide range of viscosities ranging from that for water ($10^{-3}\,\mathrm{Pa \cdot s}$) as the lower bound to the maximum viscosity for the tank mud ($52 \times 10^{-3}\,\mathrm{Pa \cdot s}$) as the upper bound. To simplify the inversion, we also assume that the mud viscosity and density is uniform within the borehole, as a reasonable assumption, as the mud is circulating during this drilling, uniforming the mud properties along the hole. We keep the value of viscosity so that we can fit at best the baseline of DHAP data (Fig. 2c). In Fig. 4, the fluid pumped from the surface into the borehole was assumed to be seawater ($\rho_{MW} = 1028\,\mathrm{kg/m^3}$, $\mu = 1\,\mathrm{mPa \cdot s}$). This result is quite satisfactory but the mud density used is lower than the one indicated in the daily drilling report with values ($\rho_{MW} = 1350\,\mathrm{kg/m^3}$, $\mu = 51\,\mathrm{mPa \cdot s}$). Mixing between the tank mud and seawater could have occurred in the borehole. Therefore, the parametric study for the full modeling of the DHAP considering a wide range of viscosity and density values for clean mud, between $1 - 52\,\mathrm{mPa \cdot s}$ and $1028 - 1370\,\mathrm{kg/m^3}$ respectively (Figure.A1). By slightly changing the properties of the clean mud, the model significantly overpredicts the DHAP data. Compared to the reference properties of seawater (Fig. A1a), changing slightly either clean mud density (Fig. A1c) or mud viscosity (Fig. A1b), the model overpredicts the baseline of the DHAP data. If the mud properties of the drilling report are applied (Fig. A1d), the model overpredicts the DHAP data by more than 3 MPa.

To quantify the quality of the fit for the whole range of values considered in the parametric studies, we used $L_2 = \frac{1}{z_{decollement}} \int_0^{z_{decollement}} \sqrt{(DHAP(z) - Pred(z))^2} * dz$ to normalize the error for the DHAP prediction above décollement. The equation L_2 is based on the principle of the distance between two points in a two-dimensional plane. The result (Figures A1 e and f) of varying slightly the density or viscosity properties of the clean mud does not show significant pressure decay. It fits within a narrow range with a normalized pressure error close to $0\,\mathrm{MPa}$, while the mud (drilling report parameters) is completely over predicted with an error close to $0.06\,\mathrm{MPa}$.

The effect of slightly varying the density or viscosity properties of clean mud in the DHAP model is not easily differentiated from this (Fig. A1e & f). However, this is already identified in Fig. A1b & c when compared with the clean mud (Fig. A1a). The parametric study shows that the model is in good agreement with empirical DHAP data only if the parameters (clean fluid density, viscosity) are close

816 to the seawater data. Therefore, this disputes the mud properties provided by the daily drilling reports
817 that earlier suggested that the mud used for drilling hole C0024A is more denser and viscous.

A3 Pore pressure prediction from d-exponent method using drilling data

A3.1 d_{xc}-exponent theory

In drilling engineering the d-exponent (d_x) method delineates the empirical relationship between rock strength, bit size, and formation drillability (Bingham, 1965). Pore pressure increase is estimated by accounting for the normalisation of the rate of penetration (ROP). In typical normal compacted sediments under hydrostatic conditions the ROP should follow an exponential decay law with depth i.e it becomes difficult to drill through highly compacted sediments.

Higher pore pressure facilitates rock failure and ROP increases rapidly (Zhang & Yin, 2017) or decreases at a slower rate than it would normally decrease in normal compacted materials. During drilling, the penetration rate is influenced by the lithological variation, the weight on the bit (WOB), the pore pressure, the rotation rate of the drill string (RPM), the torque and the type of the bit. Jorden & Shirley (1966) noted that under variable drilling conditions, there is a recognizable relationship between d-exponent and differential pressures (the bottom-hole pressure difference between the formation and the mud column):

$$d_x = \frac{\log\left(\frac{\mathrm{ROP}}{60\,\mathrm{RPM}}\right)}{\log\left(\frac{12\,\mathrm{WOB}}{10^6\ d_b}\right)} \tag{A.1}$$

Where d_x is the d exponent (dimensionless), ROP (ft / h), RPM is the rotary speed (rpm), WOB is the downhole weight on the bit (lbf) and d_b is the bit diameter (in). The original English units are retained here only for the sake of consistency. The d-exponent increases with increasing depth for a lithology, with constant bit type, mud overbalance, and increasing compaction. Trend deviations of d-exponent can be experienced when drilling through overpressured zones and by varying mud density due to overbalance. To remove the effect of mud density changes for d-exponent to respond predictably to pore pressure gradient, Rehm & McClendon (1971) proposed a correction to d-exponent called d_{xc} described in equation below:

$$d_{xc} = d_x \left(\frac{\rho_{MW}}{\mathrm{ECD}}\right) \tag{A.2}$$

Where ρ_{MW} is the clean mud density ($\mathrm{g/cm^3}$), and ECD is the equivalent circulating density. ECD provides an intuitive way to interpret the fluid pressure (DHAP), which increases steadily with depth (Fig. 2c). The estimated ECD is a key input for the Eaton d-exponent computation for pore pressure calculations. It was adapted for a riserless hole:

$$ECD = \frac{DHAP - P_{sea}}{g\ Z} \tag{A.3}$$

Where P_{sea} is the pressure at the mudline (seafloor), Z is the true vertical depth (TVD) in meter below seafloor (mbsf) and g is acceleration due to gravity (9.81 $\mathrm{m/s^2}$). The overburden gradient (σv_g) and

the hydrostatic pressure gradient (P_{hg}) are calculated:

$$P_{hg} = \rho_w\, g \tag{A.4}$$

$$\sigma v_g = \frac{\int_0^Z \rho_b(Z)\, dZ}{Z}\, g \tag{A.5}$$

Jorden & Shirley (1966) proposed that the pore pressure gradient (P_{pg}) could be determined from the d-exponent, the overburden gradient (σv_g) and the hydrostatic pressure gradient (P_{hg}).

$$P_{pg} = \sigma v_g - (\sigma v_g - P_{hg}) \left(\frac{d_{xc}}{d_n}\right)^n \tag{A.6}$$

$$d_n = d_0 + d\, Z \tag{A.7}$$

$$P_f = P_{sea} + P_{pg} Z \tag{A.8}$$

Where d_n is the normal compaction trend (NCT), n is an empirical exponent (normally $n = 1.2$ (Zhang & Yin, 2017)), d_0 is the shale d-exponent value at the mudline (seafloor), d is calibration parameter, Z is the true vertical depth below mudline (m).

A3.2 Pore Pressure d_{xc}-exponent Results

The d_{xc} line does not follow the NCT in Fig. A3b in the depth range of 0-180mbsf (coincides with part of subunit 1a [Fig. A3a]). This interval was not considered when constructing the NCT, because these facies are characterised by unconsolidated sediments from accreted continental or fluid-rich subducting plate sediments still undergoing possible erosional sediment unloading. Therefore, it is considered a hydrostatically pressured interval. The line d_{xc} follows the NCT line between 180-490 mbsf (which comprises part of subunits 1a, 1b & 1c). The d_{xc} trend increases linearly with is depth and vertical effective stress. With a increasing pressure between 39.37 MPa to 47.8 MPa (Fig. A3c), this depth range is also considered hydrostatically pressured, as illustrated on Fig. A3c & f). Overall, the mud pressure is higher than the pore pressure and hydrostatic pressure between 0-490 mbsf (Fig. A3 f). Therefore, the interval is considered normally pressured.

In Fig. A3b the d_{xc} begins to depart from the NCT to lower values at the depth of 490 mbsf. This depth coincides within subunit 1c (Fig. A3 a) and marks the top of the overpressured zone. Therefore, the overpressured zone is located between 490 mbsf and the bottom of the borehole. The variation in pore pressure within this depth range is influenced by the changing value of d_{xc} along the trend line. On Fig. A3b, d_{xc} gradually drops below 1, then gradually increases to a value of 1.06 at a depth of 786.4 mbsf, before decreasing to lower values (0.75) within the décollement interval. The d_{xc} method cannot be applied rigorously below the second strand of the décollement fault core, since the NCT for the sandy lithology of the footwall is not characterized. But a further decrease in d_{xc} shows the existence of higher pore pressure.

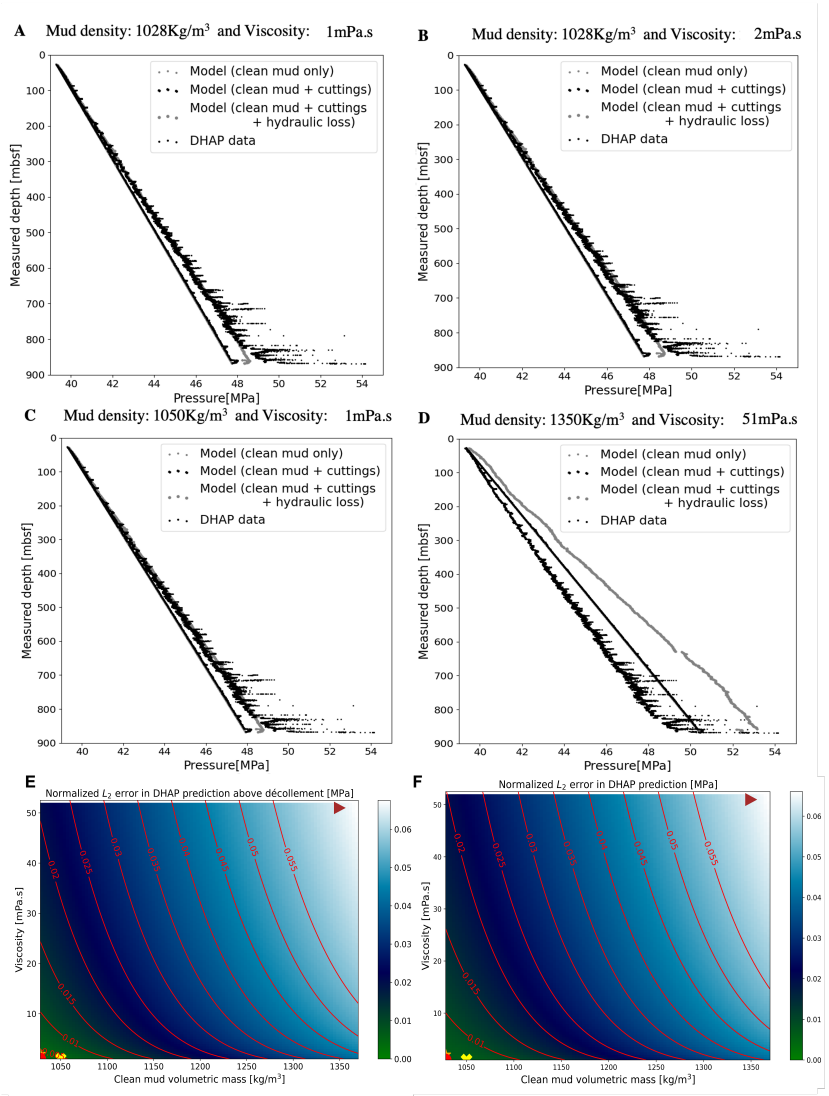

Figure A1. Parametric study of the DHAP modeling for variable mud densities and viscosity values (a) Prediction for clean mud with density $1028\ \mathrm{kg/m^3}$ and viscosity $1\ \mathrm{mPa \cdot s}$. (b) Same as (a) but with a slight change in viscosity $2\ \mathrm{mPa \cdot s}$. (c) Same as (a) but with a slight change in density of $1050\ \mathrm{kg/m^3}$ and fixed viscosity $1\ \mathrm{mPa \cdot s}$. (d) Same as (a) with the properties of the mud incorrectly stated in the drilling report with density of $1350\ \mathrm{kg/m^3}$ and viscosity of $51\ \mathrm{mPa \cdot s}$. (e) Normalized error L_2 of the DHAP prediction above décollement, for a range of different mud properties. The colored dots correspond to the profiles illustrated below: clean mud as water (dot shape), clean mud with varied density (diamond shape), clean mud with varying viscosity (x filled shape), and drilling report mud properties (triangle right shape). (f) Normalized L_2 error for the DHAP prediction for entire borehole length with varying mud properties indicated with coloured dots as in (e).

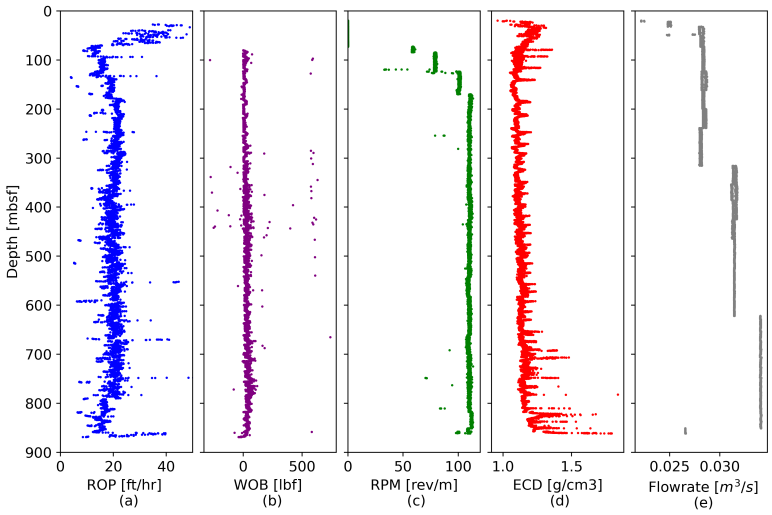

Figure A2. The input data used for the calculation of d_{xc} exponent from figure [a-d] and the figure [e] is pumping rate used as the main input data for calculation of the hydraulic loss: (a) rate of penetration (ROP) (b) weight on bit (WOB) (c) revolution per minute (RPM) (d) The equivalent circulating density (ECD), (e) Pumping rate (Q_{pump}).

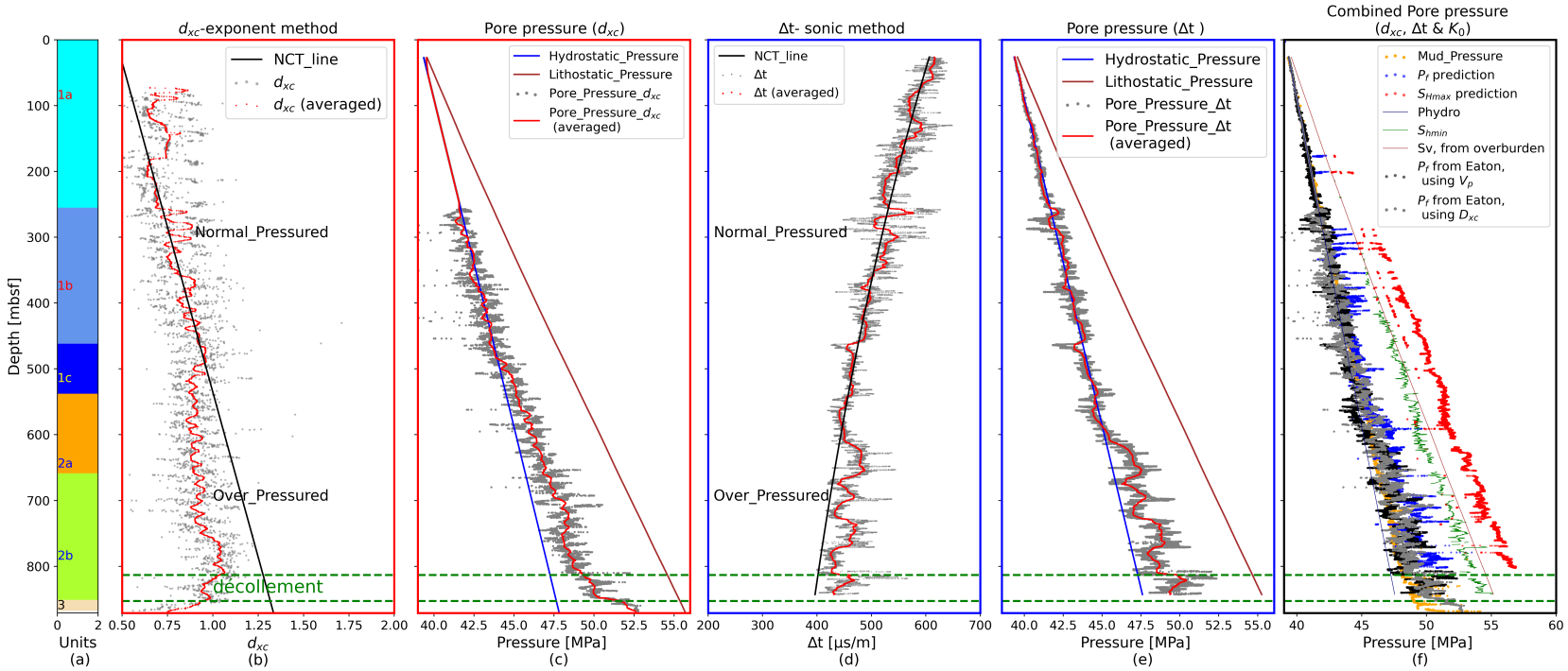

Figure A3. Pore pressure predictions from the d_{xc} exponent (red coloured rectangular frame plots [b & c]) and Δt sonic (blue coloured rectangular framed plots [d & e]) and Kitajima & Saffer (2012); Kitajima et al. (2017) method. (a) Logging units (b) Profile of the Eaton d_{xc} coefficient (raw d_{xc} [gray] and d_{xc} averaged sampled for 500 points[red]) along the borehole with an observable deviation to lower values from the NCT line (black) at the top of the subunit 1c (accreted wedge Facies). This particular depth marks the top of the overpressured interval. (c) The pore pressure profile (red line) follows hydrostatic pressure (blue line) within the normal pressured zone and rises significantly above the hydrostatic pressure within the overpressured zone. (d) Profile of the Eaton coefficient Δ t (raw Δ t [gray] and sampled Δt [red]) along the borehole with an observable deviation to higher values from the NCT line (black) within the upper Shikoku facies. (e) The pore pressure profile (red line) follows hydrostatic pressure (blue line) within the normal pressured zone and rises significantly above the hydrostatic pressure within the overpressured zone. (f) Overlay comparing both pore pressure results from Eaton's methods and Kitajima & Saffer (2012); Kitajima et al. (2017) method. The two pressure profiles (d_{xc} in gray and Δt in black) almost overlap near the décollement with a localized increase in the pore pressure across the strands while K_0 uniaxial loading pore pressure result in blue color.

The pore pressure gradually rises and at the depth of 510.8 mbsf, a crossover between the pore pressure and the DHAP is observed (Figure A3 f). This point marks the onset of higher pore pressure values over the mud pressure and it rises gently to maximum value of 52.6 MPa (Figure A3f) with localized pore pressure gradient (Figure A3c) rising up to 1.05-1.6 $\mathrm{g/cm^3}$. This method shows that the excess pore pressure ranges $P^* \approx 0.1 - 4.79$ MPa above the hydrostatic pressure and the lithostatic load ($\lambda \approx 0.54 - 0.66$, $\lambda^* \approx 0.1 - 0.62$), with lower range values within the accreted sediments and maximum values below the décollement and the underthrusting sediments ($P^* \approx 2.38 - 4.79$ MPa, $\lambda \approx 0.66 - 0.8$, $\lambda^* \approx 0.28 - 0.62$). There is localized step in pressure (Figure A3c & f) when crossing the fault core of the décollement (813 mbsf and 852 mbsf).

A4 Pore pressure prediction using sonic transit time method

A4.1 Eaton method for sonic velocities

From the relationship between seismic velocity and effective stress, Bowers (1995) postulated that the pore pressure can be estimated from the ratio between effective stress and the velocity in normally pressured sediments. Compressional velocity depends on the grain type, fluid content, and porosity of the different lithologies (Eaton, 1972). The variability of the overburden stress gradients (Terzaghi et al., 1968) depends on the region of study but is generally a function of the burial depth and the pressure gradients of the pores. Pore pressure gradient can then be estimated considering the shale travel time:

$$P_{pg} = \sigma v_g - (\sigma v_g - P_{hg}) \left(\frac{\Delta t_n}{\Delta t} \right)^m \tag{A.9}$$

Where Δt is transit time in shales from well log, Δt_n is transit time in shales (normal pressure condition), m is an exponent (empirically m is equal to 3). Departure of the sonic slowness away from the NCT to higher values indicates evidence of overpressure but true if within the same lithology. To estimate the NCT of shale travel time, we first preprocess the sonic transit time log by filtering and smoothing the data. The NCT (Δt_n) was generated by fitting an exponential relationship of the sonic travel time in relation to the drilled depth:

$$\Delta t_n = \Delta t_m - (\Delta t_{ml} - \Delta t_m)\, e^{-cz} \tag{A.10}$$

Where Δt_m is the transit time in the shale matrix, Δt_{ml} is the transit time at the mudline ($Z = 0$), Z is the true vertical depth below the mudline (mbsf), and c is the compaction parameter. The pore pressure is estimated using equation A.8.

A4.2 Pore pressure determined from sonic transit time

The sonic transit time follows the NCT (Fig. A3d) between the depth range of 0 to $580\ \mathrm{mbsf}$. It coincides with Unit 1 (accretionary trench wedge facies) and the upper part of Subunit 2a (upper part of Shikoku basin hemipelagic-pyroclastic facies) (Fig. A3a). With a increasing pressure between 39.37 MPa to $47.8\ \mathrm{MPa}$ (Fig. A3e), this depth range is also considered hydrostatically pressured, as illustrated in Fig. A3e). Overall, the mud pressure is above pore pressure (Fig. A3f) and the hydrostatic pressure between 0-580 mbsf. Therefore, this is considered a normal pressured interval.

The Δt line departs significantly from the NCT to higher increasing slowness of transit time in this lithologies at a depth of 580 mbsf (Fig. A3e). The depth coincides with the upper part of the Shikoku basin facies (Fig. A3a) and it marks the top of the geopressurized zone. Therefore, the overpressure zone is defined as the depth range between 580 mbsf and 871 mbsf (bottom of the borehole). The pore pressure gradually increases and at a depth of 611 mbsf, a crossover between the pore pressure and the DHAP is observed in Fig. A3f. This point marks the onset of higher pore pressure values over the mud pressure and it rises gently to maximum value of $50.83\ \mathrm{MPa}$ (Fig. A3f).

This method shows that the excess pore pressure ranges $P^* \approx$ 0.05–3.03 MPa above hydrostatic pressure and lithostatic load ($\lambda \approx$ 0.54-0.66, $\lambda^* \approx$ 0.1-0.41), with the lowest range values within the accreted sediments and maximum values below the décollement and the underthrusting sediments (P^* $\approx 2.57 - 3.03\ \mathrm{MPa}$, $\lambda \approx 0.63 - 0.72$, $\lambda^* \approx 0.34 - 0.41$). There is localized step in pressure (Figure A3e & f) when crossing the fault core of the décollement ($813\ \mathrm{mbsf}$) into the first asymmetric damage zones of the footwall as observed using the d-exponent method (Figure A3e).